Physiomimetic biocompatibility evaluation of directly printed degradable porous iron implants using various cell types

Li, Y.; Pavanram, P.; Bühring, J.; Rütten, S.; Schröder, K. U.; Zhou, J.; Pufe, T.; Wang, L. .; Zadpoor, A. A.; Jahr, H.

DOI
10.1016/j.actbio.2023.07.056

Publication date
2023

Document Version
Final published version

Published in
Acta Biomaterialia

Citation (APA)
Li, Y., Pavanram, P., Bühring, J., Rütten, S., Schröder, K. U., Zhou, J., Pufe, T., Wang, L. ., Zadpoor, A. A., & Jahr, H. (2023). Physiomimetic biocompatibility evaluation of directly printed degradable porous iron implants using various cell types. *Acta Biomaterialia*, *169*, 589-604. https://doi.org/10.1016/j.actbio.2023.07.056

Acta Biomaterialia 169 (2023) 589–604

Contents lists available at ScienceDirect

Acta Biomaterialia

journal homepage: www.elsevier.com/locate/actbio

Full length article

Physiomimetic biocompatibility evaluation of directly printed degradable porous iron implants using various cell types

Y. Li[a,b,1,*], P. Pavanram[c,1], J. Bühring[d], S. Rütten[e], K-U. Schröder[d], J. Zhou[b], T. Pufe[c], L-N. Wang[a,*], A.A. Zadpoor[b], H. Jahr[c,d,*]

[a] Beijing Advanced Innovation Center for Materials Genome Engineering, School of Materials Science and Engineering, University of Science and Technology Beijing, Beijing, 100083, China
[b] Department of Biomechanical Engineering, Delft University of Technology, Delft 2628CD, the Netherlands
[c] Institute of Anatomy and Cell Biology, University Hospital RWTH Aachen, Aachen 52074, Germany.
[d] Institute of Structural Mechanics and Lightweight Design, RWTH Aachen University, 52062 Aachen, Germany
[e] Institute of Pathology, Electron Microscopy Unit, University Hospital RWTH Aachen, Aachen 52074, Germany

ARTICLE INFO

Article history:
Received 4 March 2023
Revised 4 July 2023
Accepted 27 July 2023
Available online 1 August 2023

Keywords:
Additive manufacturing
Porous iron
Perfusion bioreactor
Biodegradation
Biocompatibility
MG-63, L929, HUVEC, RAW264.7

ABSTRACT

Additively manufactured (AM) degradable porous metallic biomaterials offer unique opportunities for satisfying the design requirements of an ideal bone substitute. Among the currently available biodegradable metals, iron has the highest elastic modulus, meaning that it would benefit the most from porous design. Given the successful preclinical applications of such biomaterials for the treatment of cardiovascular diseases, the moderate compatibility of AM porous iron with osteoblast-like cells, reported in earlier studies, has been surprising. This may be because, as opposed to static *in vitro* conditions, the biodegradation products of iron *in vivo* are transported away and excreted. To better mimic the *in situ* situations of biodegradable biomaterials after implantation, we compared the biodegradation behavior and cytocompatibility of AM porous iron under static conditions to the conditions with dynamic *in situ*-like fluid flow perfusion in a bioreactor. Furthermore, the compatibility of these scaffolds with four different cell types was evaluated to better understand the implications of these implants for the complex process of natural wound healing. These included endothelial cells, L929 fibroblasts, RAW264.7 macrophage-like cells, and osteoblastic MG-63 cells. The biodegradation rate of the scaffolds was significantly increased in the perfusion bioreactor as compared to static immersion. Under either condition, the compatibility with L929 cells was the best. Moreover, the compatibility with all the cell types was much enhanced under physiomimetic dynamic flow conditions as compared to static biodegradation. Our study highlights the importance of physiomimetic culture conditions and cell type selection when evaluating the cytocompatibility of degradable biomaterials *in vitro*.

Statement of Significance

Additively manufactured (AM) degradable porous metals offer unique opportunities for the treatment of large bony defects. Despite the successful preclinical applications of biodegradable iron in the cardiovascular field, the moderate compatibility of AM porous iron with osteoblast-like cells was reported. To better mimic the *in vivo* condition, we compared the biodegradation behavior and cytocompatibility of AM porous iron under static condition to dynamic perfusion. Furthermore, the compatibility of these scaffolds with various cell types was evaluated to better simulate the process of natural wound healing. Our study suggests that AM porous iron holds great promise for orthopedic applications, while also highlighting the importance of physio-mimetic culture conditions and cell type selection when evaluating the cytocompatibility of degradable biomaterials *in vitro*.

1. Introduction

Treating large bone defects with synthetic open-porous 3D scaffolds can overcome the current limitations of autologous bone grafting [1]. Additive manufacturing (AM) provides unprecedented

* Corresponding authors.
E-mail addresses: yagengli@ustb.edu.cn (Y. Li), luning.wang@ustb.edu.cn (L-N. Wang), hjahr@ukaachen.de (H. Jahr).
[1] Authors contributed equally.

https://doi.org/10.1016/j.actbio.2023.07.056
1742-7061/

opportunities for precise control of the geometries and micro-architected structures of such scaffolds. AM porous metallic biomaterials, such as cobalt chromium, stainless steel, or titanium exhibit mechanical properties that are similar to the human cortical bone [2] and can be applied in load-bearing areas [3]. Due to its outstanding mechanical properties and biocompatibility, Ti-6Al-4V (Ti64) is considered a standard of care and is commonly used in orthopedic applications like clavicular, mandibular, and acetabular implants [4,5]. However, such bio-inert metallic biomaterials may lead to permanent physical irritation [6], chronic local inflammation [7], implant-associated infections [8], and incomplete bone regeneration [9], which may necessitate revision surgery [10]. Ideal bone-substituting scaffolds for bone defect repair and regeneration should, therefore, be biodegradable, providing enough mechanical and bio-functional support upon implantation while degrading gradually as the bone regenerates [11].

Iron (Fe) is one of the three most promising biodegradable metals, but has attracted less attention than magnesium and zinc [12]. Due to its high elastic modulus, strength, and biocompatibility, it has been found to be an appropriate candidate for cardiovascular applications [12]. As compared to magnesium and zinc, the biodegradation rate of iron is much lower [13–15]. Many studies aim at increasing the biodegradation rate of iron through alloying [16]. However, increased volumetric porosity may be a better way to achieve a higher rate of biodegradation through an enlarged reactive surface area while also providing room for bony ingrowth and avoiding the presence of any cytotoxic alloying elements. Importantly, the relatively high elastic modulus and strength of Fe leaves a sufficient scope for introducing substantial porosity. We, and others, have already demonstrated the potential of AM Fe and Fe-based alloys as promising temporary bone replacement biomaterials that degrade at an adequate pace to allow for gradual load transfer from the scaffold to the regenerating bone tissue [13,17-19]. Geometrical features (*e.g.*, pore size, pore shape, and porosity) of Fe scaffolds can be precisely controlled through AM [20,21]. The design of such micro-architected structures not only determines their mechanical properties, but can also adjust their biodegradation rates [20] and affect cell attachment, extracellular matrix (ECM) deposition, and subsequent vascularization.

Fe has exhibited no signs of cytotoxicity during long-term implantation as biodegradable stents or pins [22–25], but *in vitro* biocompatibility results contradict each other [26–28]. Our body's sophisticated secretion system ensures the disposal of waste products through the kidneys and the urinary system [29]. In contrast to this dilution of locally released ions by interstitial and intravascular fluids *in vivo*, static *in vitro* testing contains and concentrates locally released ions [30]. *In vitro* static incubation can, therefore, not accurately predict the *in vivo* corrosion rates of biodegradable scaffolds [31]. New biomaterials must pass cytocompatibility tests prior to their pre-clinical evaluation *in vivo*. While ISO 10993 is often used for such cytocompatibility evaluation [32], it is only relevant for inert biomaterials and was never meant to be used for biodegradable biomaterials. To better mimic the *in vivo* situation *in vitro*, ISO 10993 has been modified through EN ISO 10993-5 and 10993-12 in which such measures as using a 10-times higher extraction ratio are suggested for biodegradable metals [33,34]. Furthermore, culture conditions can significantly affect the results of *in vitro* cytocompatibility assays [35]. Indeed, a more complex *in vitro* set-up mimicking some of the biologically relevant *in vivo* conditions is needed for more accurate assessment of biodegradable biomaterials [36]. Finally, the selected cell type may play an important role in determining the outcome of *in vitro* cytotoxicity assays, highlighting the need for a multi-cellular approach [37]. For example, good *in vitro* compatibility with calvaria-derived murine osteoblast-like MC3T3-E1 cells has been reported in static cultures for 3D printed iron-manganese scaffolds [28]. Similar observations are made regarding the compatibility of 'bare' Fe with MG-63 cells [38]. However, we have previously shown that AM porous Fe exhibits less favorable compatibility with MG-63 osteoblast-like cells [13]. Other studies with different cell types have obtained similar results using direct contact assays on iron alloys [26,27].

In this study, we address the abovementioned shortcomings of *in vitro* cytocompatibility assays to paint a more complete picture of the biocompatibility of AM biodegradable porous iron and pinpoint the source of inconsistency between previous studies. As most tissues comprise multiple types of cells, *in vitro* cytocompatibility tests should consider different cell types of relevant origins [39,40]. The healing of bony fractures involves monocytic inflammatory cells (*i.e.*, macrophages), bone cells, mesenchymal progenitor cells, endothelial cells, and potentially fibroblasts [41]. Here, we comparatively evaluated the compatibility of 3D-printed porous Fe scaffolds with murine macrophages (RAW264.7), murine fibroblasts (L929), human osteoblasts (MG-63), and human endothelial cells (HUVEC). In addition, only a few described dynamic fluid flow bioreactor systems for cytotoxicity testing that could better recapitulate the interstitial fluid transport *in vivo* than static culture conditions [42,43]. We, therefore, used a bioreactor-based dynamic, *in vivo*-mimetic biodegradation and biocompatibility evaluation system to reveal cell type- and test condition-specific outcomes.

2. Materials and methods

2.1. Scaffold manufacturing and topological characterization

AM Fe scaffolds were designed using the software nTopology (nTopology, USA) with a height of 11.2 mm and a diameter of 10 mm. The structural design was based on diamond unit cells with a strut thickness of 0.4 mm, a pore size of 0.6 mm, and a cell size of 1.4 mm (Fig. 1a, b). The as-built scaffolds were produced with a ProX DMP 320 machine (3D Systems, Belgium) using nitrogen gas atomized Fe powder as described in detail in our earlier work [13]. Fe scaffolds were then detached from the substrate plate through electrical discharge machining (EDM) and were ultrasonically cleaned to remove entrapped powder particles.

Micro-computed tomography (μCT) (Quantum FX, Perkin Elmer, USA) and Analyze 11.0 (Perkin Elmer, USA) reconstruction software were applied to investigate the morphological characteristics of the as-built specimens. The average strut thickness, pore size, and surface area were calculated using BoneJ: a plugin of FIJI (NIH, Bethesda, MD, USA). More detailed information about the parameters and methods used for topological characterization can be found in our earlier publication [13].

2.2. Static and dynamic biodegradation tests

Both static and dynamic *in vitro* biodegradation tests were performed for 1, 7, 14, and 28 days inside an incubator under physiological conditions (37 °C, 20% O_2, 5% CO_2, and 95% humidity) using the revised simulated body fluid (r-SBF) [44]. Dynamic tests were performed in a custom-built bioreactor used in our previous study [20]. To mimic the physiological fluid flow pattern seen in the human bone, a flow rate of 0.3 ml/min was used in the bioreactor [45]. At different time points during the static and dynamic biodegradation tests, the weight loss and pH were measured as previously described [39,46]. The concentrations of Fe, Ca, and P ions in the solution were analyzed at different time points using an inductively coupled plasma optical emission spectroscope (ICP-OES, iCAP 6500 Duo, Thermo Scientific). Osmolality variation in the r-SBF at different time points were analyzed using an osmometer (OSMOMAT 030, Berlin, Germany).

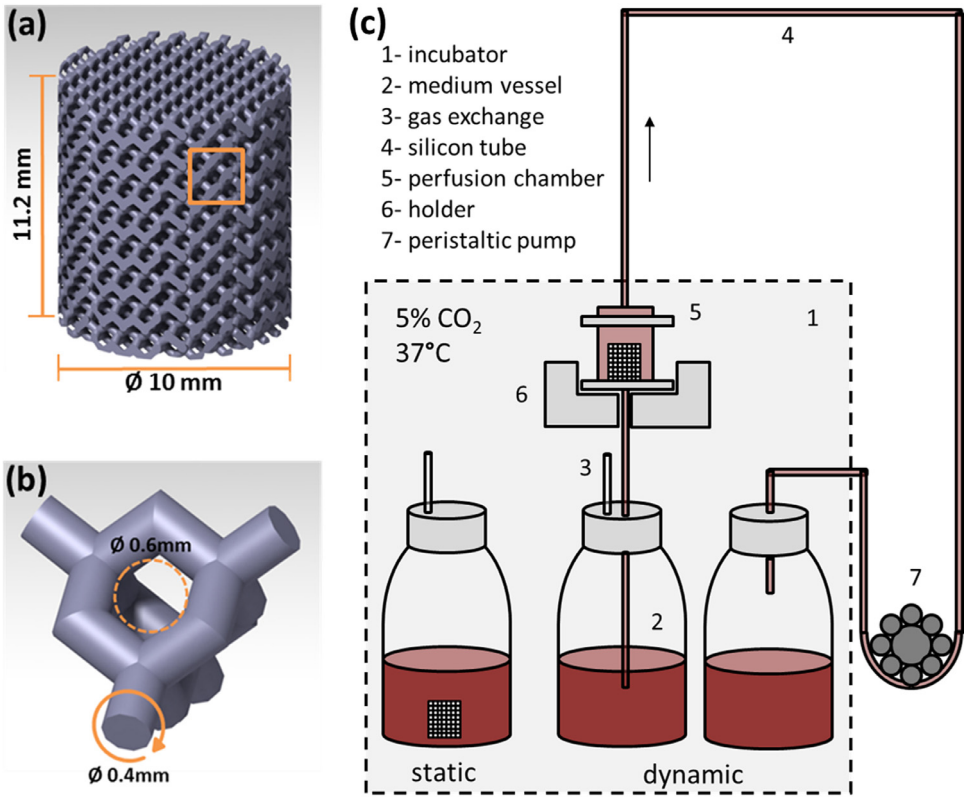

Fig. 1. The design of the specimens and a schematic drawing of the dynamic perfusion bioreactor setup for the biocompatibility testing of porous iron scaffolds (**a**), diamond unit cell design (**b**), and static and dynamic physiomimetic biocompatibility testing (**c**). The arrow indicates the direction of the medium flow.

2.3. Characterization of biodegradation products

The morphologies and compositions of the biodegradation products on the surface of the specimens after static and dynamic biodegradation tests were analyzed with a scanning electron microscope (SEM) equipped with an energy-dispersive X-ray spectroscope (EDS) (JSM-IT100, JEOL). In addition to observing the biodegradation products, the specimens were ultrasonically cleaned in ethanol to observe the morphologies of the struts after *in vitro* biodegradation.

2.4. Cell culture

The biocompatibility of the AM iron specimens was tested using four different cell lines of bone (MG-63, CRL-147, ATCC, USA), fibroblast (L929, CCL-1, ATCC, USA), endothelial (HUVEC, C12250, PromoCell, Heidelberg, Germany), and macrophage (RAW 264.7, TIB-71, ATCC, USA) cells. The MG-63 cells were cultured in the Dulbecco's modified eagle medium (DMEM) with a low glucose concentration of 1000 mg/L (DMEM LG, Sigma-Aldrich, Steinheim, Germany), L929 cells were cultured in DMEM HG (high glucose concentration of 4500 mg/L, Sigma-Aldrich, Steinheim, Germany), HUVEC cells were cultured in endothelial cell growth medium (C-22010, Promocell, Heidelberg, Germany), and RAW 264.7 cells were cultured in DMEM HG. All the cell types except for HUVEC were cultured in 10% fetal calf serum (FCS, PAN Biotech, Aidenbach, Germany) under physiological conditions. For all the biocompatibility experiments, cleaned specimens were sterilized for 30 min using 100% isopropanol (Merck; Darmstadt, Germany).

2.5. Cell seeding efficiency

The seeding efficiency of the different cell types (MG-63, L929, HUVEC and RAW 264.7) on Fe scaffolds was assessed in triplicates ($n = 3$). Cell suspensions (250,000 cells per mm height) were added dropwise to the specimens placed in 48-well plates. After 30 min, 1 ml of medium was slowly added, and the specimens were further incubated for 6 h under static physiological conditions prior to transferring them into a fresh 48-well plate. The remaining cells in the wells, not attached to scaffolds, were counted [47,48] and the cell seeding efficiency was calculated using the equation:

$$\text{Cell seeding efficiency } (\%) = \frac{(\text{initial cells added to scaffold} - \text{remaining cells in wells})}{\text{initial cells added to scaffold}} \text{ X } 100$$

2.6. DNA measurement

The cell-seeded Fe scaffolds (250,000 cells per mm height) were washed with 1× PBS following 24 h of incubation under physiological conditions and were lysed by subsequent freeze-thaw cycles (3 times) in 1× TE buffer with 0.2% Triton™ X-100 (Sigma-Aldrich, Steinheim, Germany). The Quanti-iT Picogreen dsDNA assay kit (Invitrogen, Carlsbad, USA) was used to quantify the DNA content of the specimens. A 200-fold diluted pico green solution was prepared as per manual instructions and 100 µl of this was added to 100 µl of the cell lysates. After 3 min of incubation, the intensity was measured using a multi-plate reader (Tecan Infinite M200 Plate Reader, Mainz, Germany) at the excitation and emission wavelengths of 480 and 520 nm, respectively. The florescence intensity was converted to DNA concentration using the DNA standard curve as per the manufacturer's instructions. The values are presented as mean ± SD of three independent measurements ($n = 3$) [49].

2.7. Indirect, extract-based cytotoxicity evaluation in vitro

The MG-63, RAW 264.7, HUVEC, and L929 cells were used to evaluate the cytotoxicity of the extracts associated with the AM Fe specimens. We have previously described the methodology for the preparation of the extracts and MTS assay [13]. Briefly, extracts of 0.2 g/ml concentration (1×) were prepared by incubating the Fe scaffolds for 72 h (recommended by EN ISO standards 10993:5 and 10993:12) in the respective cell-specific culture medium. The cells were treated with 10× diluted extracts of Fe for different incubation times (*i.e.*, 0, 24, 48 and 72 h). A 1× extract prepared from Ti6Al4V scaffolds with the same design and 20% dimethyl sulfoxide (DMSO) served as the positive and negative controls, respectively. The relative cellular activity was determined by using the MTS assay (CellTiter 96® AQueous One Solution Cell Proliferation Assay, G3580, Promega, Walldorf, Germany).

2.8. Direct contact biocompatibility assessment in vitro: Static vs Dynamic incubation

The biocompatibility of AM porous iron specimens was assayed using MG-63, RAW 264.7, HUVEC and L929 cells under static conditions and MG-63 and L929 cells under dynamic conditions with a custom-built setup (Fig. 1c) at a flow rate of 0.3 ml/min. The cell-seeded specimens (250,000 cells per mm height) were incubated in their respective culture medium under physiological conditions for 24 h. These scaffolds were then analyzed, as described below, by fluorescent optical imaging (FOI), SEM, and flow cytometry to compare their associated cell behaviors statically and dynamically.

2.8.1. Fluorescence staining

Live-dead staining (ab115347, Abcam, Cambridge, UK) was performed on the cell-seeded scaffolds in accordance with the instructions provided by the kit manufacturer. Briefly, 5× concentration of dye was added to the cell-seeded scaffolds followed by incubation for 10 minutes at room temperature, prior to fluorescence optical imaging (FOI) of the living (emission: 495 nm, excitation: 515 nm) and dead cells (emission: 528 nm, excitation: 617 nm) [14].

2.8.2. Scanning electron microscopy

After fluorescence staining, the specimens were rinsed in 1× PBS and were fixed in 3% glutaraldehyde (Agar scientific, Wetzlar, Germany) in 0.1 M Soerensen's phosphate buffer (Merck, Darmstadt, Germany) for 1 h at room temperature. Then, the scaffolds were dehydrated in 30, 50, 70, 90 and 100% ethanol for 10 min each (the last step was performed twice). Then, the specimens were air-dried at room temperature and were sputter-coated (Sputter Coater EM SCD500, Leica, Wetzlar, Germany) with 12.5 nm of gold-palladium and were imaged in SEM (ESEM XL-30 FEG, FEI, Eindhoven, the Netherlands) at 10 kV.

2.8.3. Flow cytometry analysis

The cell-seeded Fe scaffolds incubated statically or dynamically for 24 h were washed with 1× PBS and were then trypsinized to detach the cells. After centrifugation, all the pellets were re-suspended in a medium (50% diluted with PBS) at a concentration of 0.5×10^6 cells/ml. Staining was performed according to the supplier's instructions (ab115347, Abcam, Cambridge, UK). Live-dead staining dye (1×) was added to the cell suspension followed by incubation for 10 min at room temperature. The fluorescence signal (living cells at a 495 nm emission and a 515 nm excitation and dead cells at a 528 nm emission at a 617 nm excitation) was detected with an LSRFortessa flow cytometer (BD Biosciences, Heidelberg, Germany) and was analyzed with the FlowJo V10 software (Tree Star, Inc., Ashland, USA). At least 7,000 events were acquired for each of the tested specimens. The gating process was validated with respective healthy and lysed cell controls.

2.9. Statistical analysis

The cell seeding efficiency and DNA measurement data were analyzed using one-way ANOVA test ($\alpha = 0.05$) followed by a Turkey's multiple comparison test ($\alpha = 0.05$). The cytotoxicity test data were normalized to their corresponding controls. The resulting relative cellular activities were then analyzed using two-way ANOVA ($\alpha = 0.05$) followed by a *post-hoc* test (*i.e.,* the Turkey's multiple comparison test, $\alpha = 0.05$). The flow cytometry analysis data were analyzed using one-way ANOVA test ($\alpha = 0.05$). The statistical significance is indicated as $p < 0.0001$, ****; $p < 0.001$, ***; $p < 0.05$, *; n.s. = not significant.

3. Results

3.1. Morphological characteristics of the AM Fe scaffolds

Our µCT analyses revealed that the as-built scaffolds had an average strut size of 461 ± 4 µm (design value = 400 µm) and a pore size of 506 ± 11 µm (design value = 600 µm). The surface area of the scaffolds was 27.1 ± 0.1 cm^2 (design value = 25 cm^2). The actual porosity of the specimens was calculated to be 58.4 ± 2% (design value = 67%).

3.2. In vitro biodegradation behavior of the AM Fe scaffolds

Under both static and dynamic conditions, brownish degradation products formed on the surface of the scaffolds on day 1. From day 7 to day 28, the amount of biodegradation products gradually increased (Fig. 2a). After 28 days, statically incubated specimens were more or less covered by brownish degradation products, while dynamic incubation caused the biodegradation products to precipitate gradually in the flow direction on top of the scaffolds (Fig. 2a). The biodegradation products were loosely attached to and easily peeled off from the struts of the specimens. Under dynamic conditions, the weight loss of the AM Fe scaffolds exponentially increased with immersion time from 18.8 mg on day 1 to 231.23 mg on day 28. In contrast, the weight loss under static conditions was relatively constant over time with a slightly decreasing trend from day 14 to day 28 (Fig. 2b). At each of the tested immersion time points, dynamically incubated specimens showed more weight loss as compared to the statically incubated ones (Fig. 2b). Under dynamic conditions, the concentration of the Fe ion increased from 0.425 mg/L to 4.73 mg/L over immersion time. The concentrations of Fe ion at different locations were always higher under the dynamic test conditions as compared to the static ones (Fig. 2d). As expected, osmolality also kept increasing during the whole immersion period of 28 days (Fig. 2e) during which the dynamically incubated specimens showed higher osmolality than the static ones at all the measurement time points. Interestingly, the pH values of the r-SBF solutions of dynamically and statically incubated specimens developed almost congruently over time: after an initial rise within the first day of immersion from pH 7.4 to 7.6, a plateau was reached, followed by a slight secondary acidification phase from day 14 onwards, which resulted in an ultimate pH value of ≈7.4 on day 28 (Fig. 2c).

3.3. Characteristics of degradation products

The SEM analyses of the external struts showed that, after 28 days of static immersion, a layer of biodegradation products had formed on the surface of the struts (Fig. 3a), while dynamic conditions were associated with smoother struts with less corrosion products (Fig. 3b). There were three types of morphologies of degradation products, regardless of the immersion condition. A cluster of particle-shaped degradation products containing C, O, P,

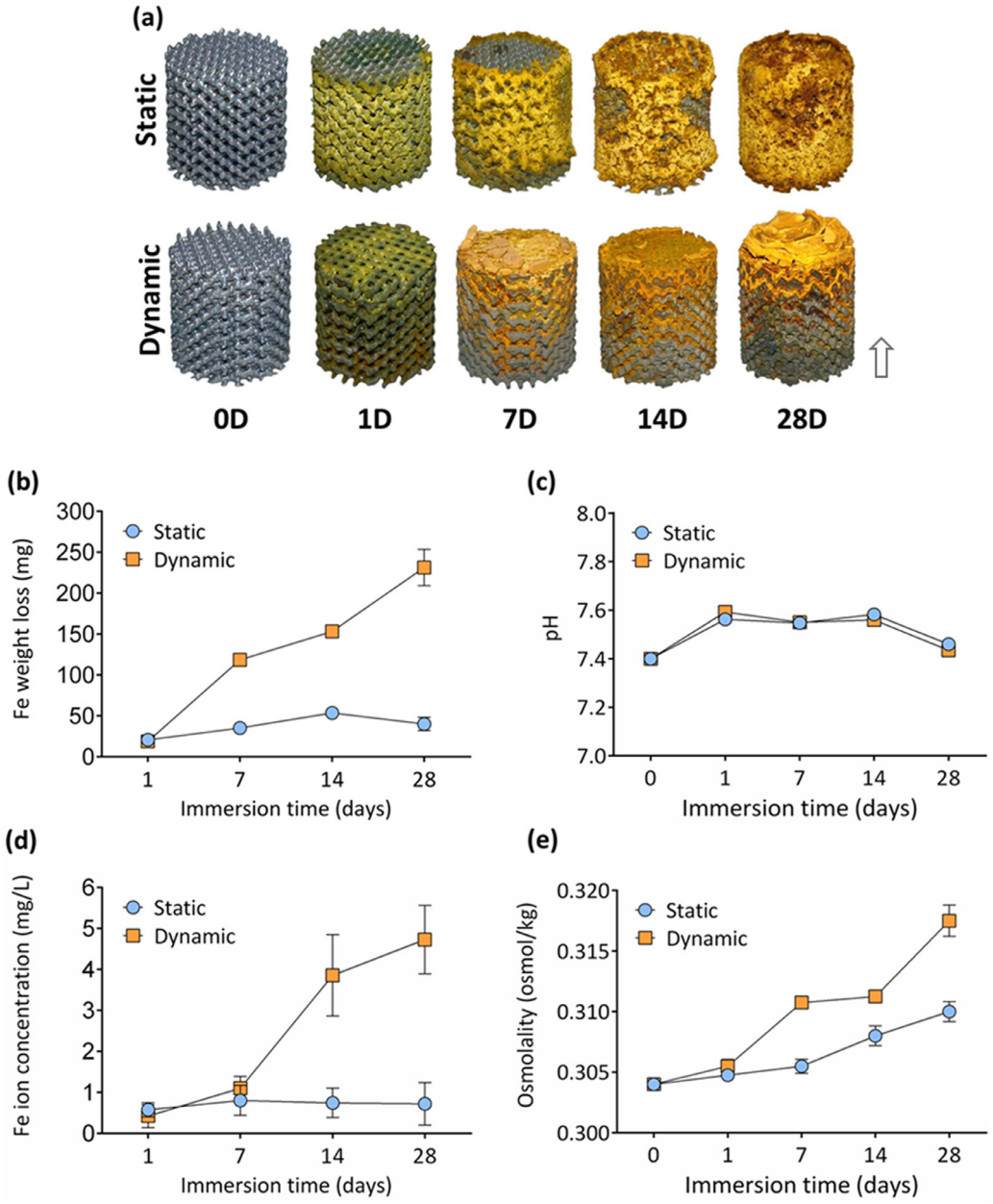

Fig. 2. Biodegradation behavior of AM porous Fe scaffolds: as-degraded scaffolds with an arrow indicating the direction of the medium flow (a), weight loss (b), pH variation with immersion (c), variation in the concentration of the Fe ion with the immersion time (d), osmolality variation with the immersion time (e). D = days of culture.

Ca, Na, and Fe were detected on both statically and dynamically incubated specimens (Fig. 3c, d). Feather-shaped biodegradation products only contained C, O, and Fe (Fig. 3e). Other biodegradation products were spherically shaped and primarily contained C, O, and Fe (Fig. 3g), with additional Ca found under the static immersion conditions (Fig. 3h).

After cleaning off the corrosion layer, the r-SBF appeared to have attacked the struts and exposed grains on their surfaces. The dynamically incubated specimens (Fig. 4b) exhibited more grain boundaries than the static ones (Fig. 4a). Some biodegradation products remained on the surface of the specimens even after cleaning (Fig. 4c, d). These residual biodegradation products contained C, O, Na, Ca, and Fe for the statically incubated specimens (Fig. 4c), while no Na was found on the dynamically incubated specimens (Fig. 4d).

3.4. General cytocompatibility

We used cell seeding efficacy as an initial measure of the biological attractiveness of the AM Fe scaffolds. The cell seeding efficiency was >75% for all the considered cell types (*i.e.*, 83% for MG-63, 91% for L929, 79% for HUVEC, and 82% for RAW 264.7 respectively). Neither the cell seeding efficiencies nor the DNA contents differed significantly (Fig. 5). The DNA content ranged between 2.21 and 6.8 μg per specimen, with the highest and lowest mean values obtained for the RAW 264.7 (5.62 μg per scaffold) and MG-63 (3.51 μg per scaffold) cells (Fig. 5b). The HUVEC and L929 cells showed mean DNA contents of 3.91 and 5.46 μg per specimen, respectively (Fig. 5b).

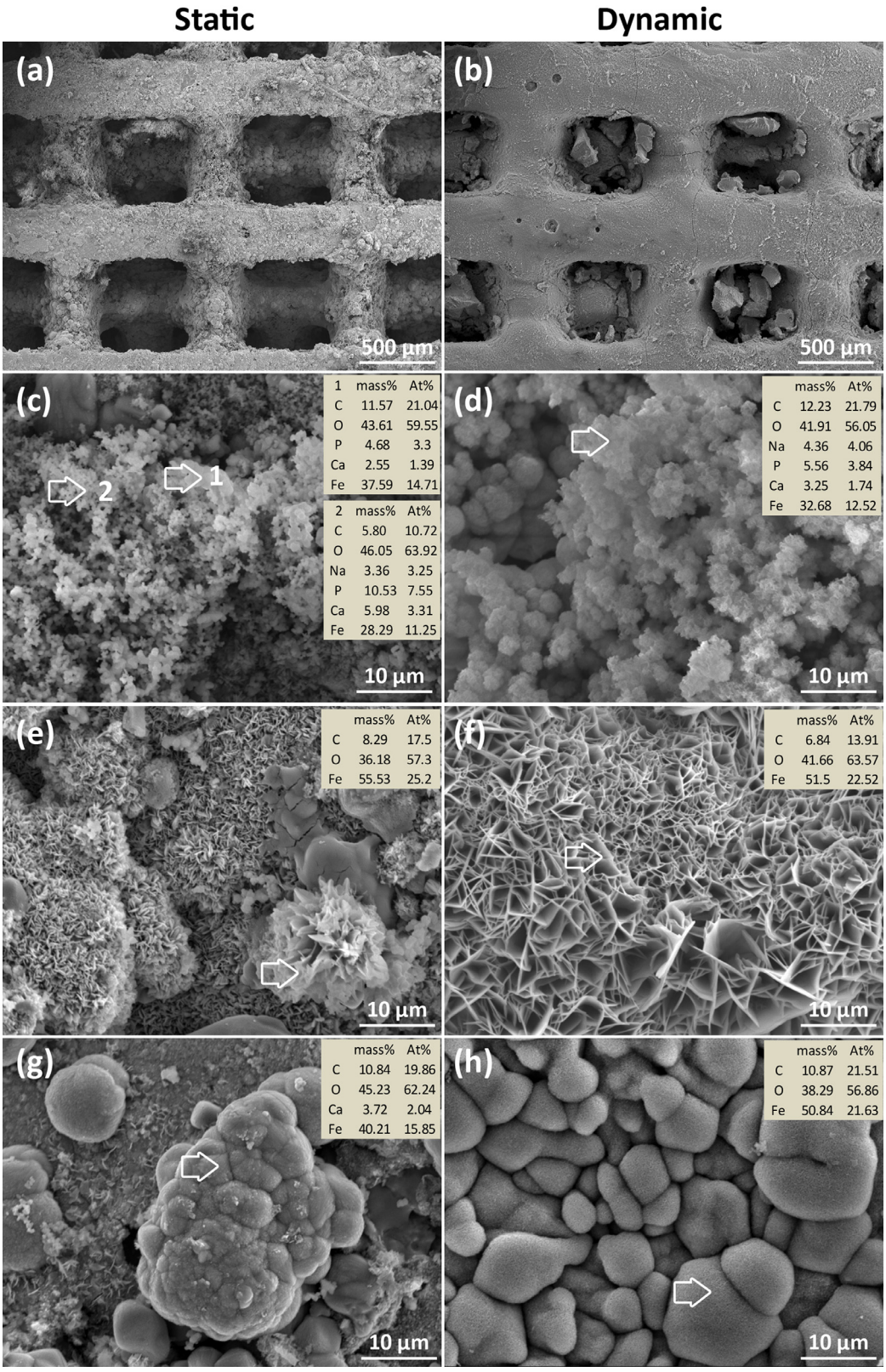

Fig. 3. The SEM and EDS analyses of the biodegradation products after 28 days of static and dynamic incubation *in vitro*: strut morphology at a lower magnification (a, b) and the degradation products formed on the surface of the specimens at a higher magnification (c-h). Arrows indicate the spots where the EDS analysis was performed.

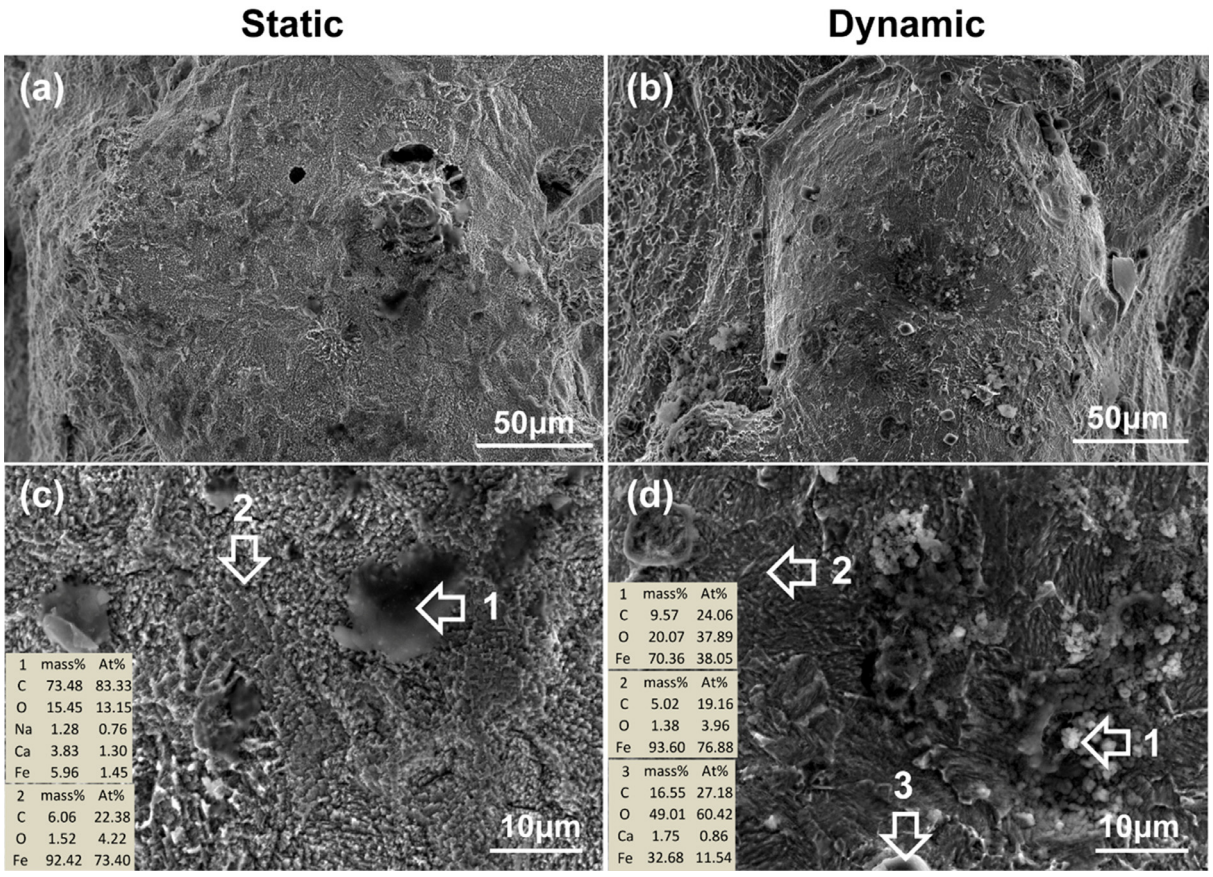

Fig. 4. The SEM and EDS analyses of the retained biodegradation products upon cleaning after 28 days of static and dynamic incubation *in vitro*: the strut morphology at a higher magnification (a, b) and the biodegradation products remaining on the surface of the specimens (c, d). Arrows indicate the spots where EDS analysis was performed.

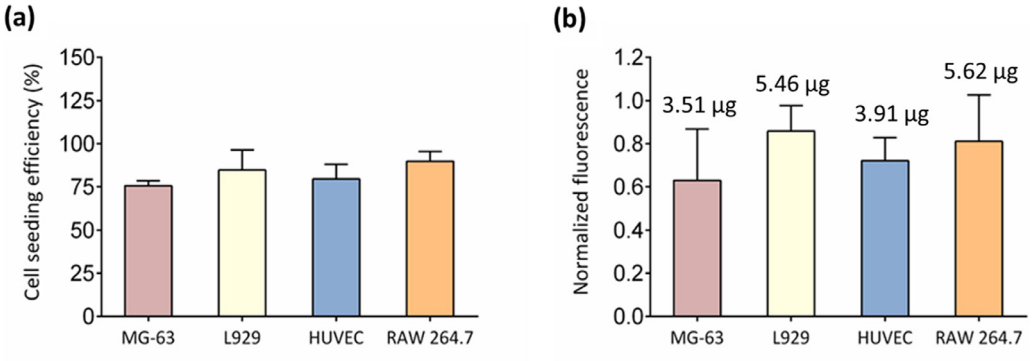

Fig. 5. The cell seeding efficiency and DNA content analyses. Four different cell types were cultured on the AM porous Fe scaffolds and (a) the percentage of the attached cells (6 h after seeding) and (b) the DNA content (normalized fluorescence; 24 h after seeding) are presented.

3.5. *Indirect, extract-based cytotoxicity evaluation* in vitro

The metabolic activity of the MG-63, L929, HUVEC and RAW 264.7 cells cultured in standardized extracts from the AM Fe scaffolds was assayed and compared to that of the extracts from identically designed Ti64 scaffolds (positive controls). Even after a prolonged incubation time of 72 h (as defined according to EN ISO standards 10993:5 and 10993:12), a high percentage (*i.e.*, 86-100%) of each tested cell type cultured in the Ti64 extracts was viable. This re-confirms the high level of cytocompatibility of Ti64 as the positive control. In contrast, the cellular activity of all the cell types quickly dropped to <60% within 24 h, and to <15% after 72 h, in the DMSO negative control (Fig. 6). In the case of the Fe extracts, the cellular activity of all the tested cell types was >70% after 24 h: 75% for MG-63 (Fig. 6a), 95% for L929 (Fig. 6b), 73% for HUVEC (Fig. 6c), and 73% for RAW 264.7 (Fig. 6d). After 48 h and 72 h, only the L929 cells retained their cellular activity at ≥85% (Fig. 6d). All the other cell types exhibited a gradual decrease in their cell viability with incubation time in the Fe extracts: ≈60% and ≈45% at 48 h and 72 h, respectively.

3.6. *Direct contact cytocompatibility* in vitro*: static* vs. *dynamic incubation*

The cytotoxic effects of direct cell contact with the surface of the Fe scaffolds were evaluated, based on the morphological changes observed in the SEM image analyses as well as the results of live-dead staining. As opposed to the static conditions (Fig. 7),

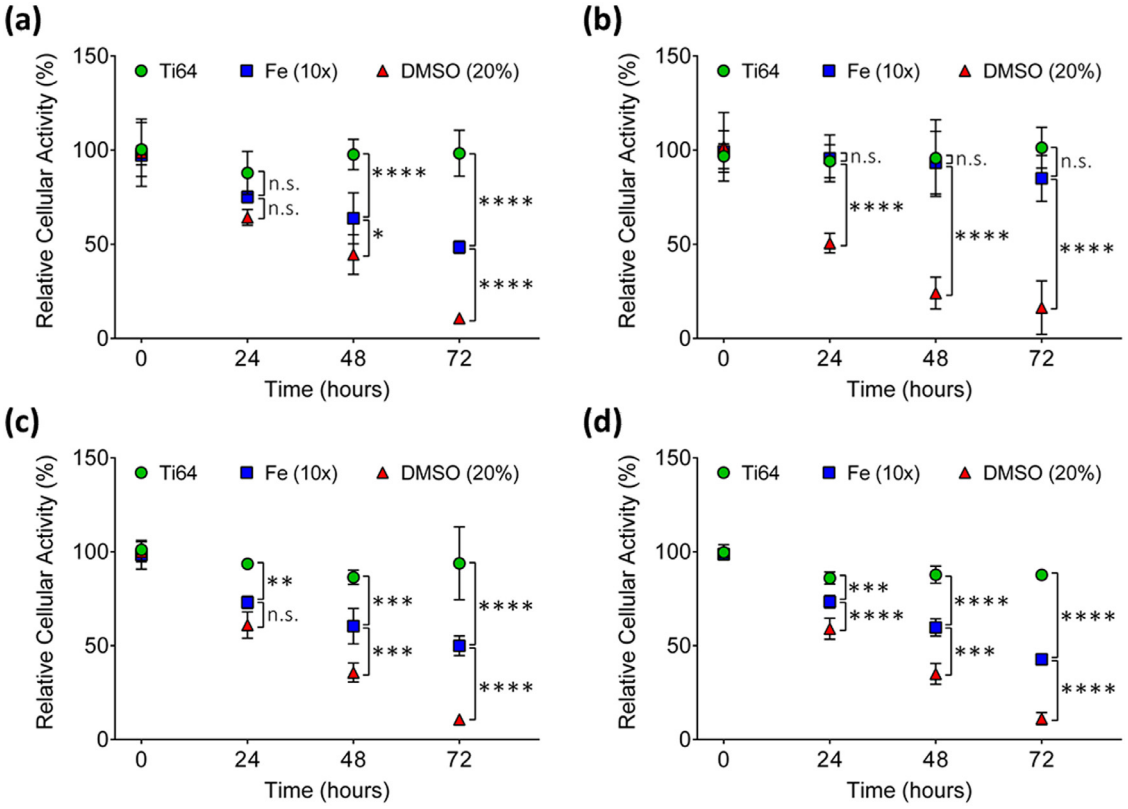

Fig. 6. The *in vitro* cytocompatibility of the AM porous Fe scaffolds: The relative cellular activity (%) of MG-63 (a), L929 (b), HUVEC (c), and RAW 264.7 (d) upon exposure to the extracts corresponding to the AM Fe scaffolds. The experiments were performed with the extracts of randomly chosen replicate iron scaffolds (blue squares, $n = 5$) and were compared to those corresponding to the AM Ti-6Al-4V (green circles, Ti64) specimens with the same design ($n = 3$). Dimethylsulfoxide (DMSO, red triangles) was used as a negative control. n.s. = not significant; *, $p < 0.05$; **, $p < 0.01$; ***, $p < 0.001$; ****, $p < 0.0001$.

the cells residing on the surface of the dynamically incubated Fe scaffolds (Fig. 8) were generally more viable and presented cell morphologies that were similar to the ones observed on the positive controls. Under the static immersion conditions, the degrees of biocompatibility of the MG-63, HUVEC and RAW 264.7 cells were similarly low, as evident from the high percentage of dead cells (Fig. 7). In contrast, after 24 h in direct contact with the Fe scaffolds, the majority of the L929 cells were still viable, with a limited number of dead cells (Fig. 7c). While a much smaller percentage of the MG-63 cells were vital (Fig. 7a), their morphological appearance (Fig. 7b) was promising. In the case of the HUVEC (Fig. 7e) and RAW 264.7 (Fig. 7g) cells, direct contact with the surface of the AM Fe specimens caused a high degree of cytotoxicity.

Under the dynamic culture conditions, the vast majority of the L929 and HUVEC cells in contact with the specimens stained vivid green and were apparently vital (Fig. 8e, i). The MG-63 and RAW 264.7cells in contact with the Fe specimens appeared almost as vital (Fig. 8a, m) as the ones in contact with the Ti64 controls (Fig. 8c, o).

Although SEM imaging (Fig. 7) revealed close contact between all the cells and the surface of the Fe struts, the cells generally exhibited a rounded morphology under the static conditions, save for L929 (Fig. 7d). Under the dynamic culture conditions (Fig. 8), the SEM images revealed an enhanced attachment of the MG-63 (Fig. 8b), L929 (Fig. 8f), HUVEC (Fig. 8j), and RAW 264.7 (Fig. 8n) cells to the surface of the AM Fe specimens. The dynamic test conditions, therefore, improved cell-biomaterial adhesion and cell-cell contacts through far-stretching filopodia-like protrusions, which was reminiscent of their appearance on Ti64 (Fig. 8d, h).

3.7. Quantification of direct contact cytocompatibility: static vs. dynamic incubation

Quantification of live-dead cells is difficult inside opaque porous metals, as stained cells can only be observed on the peripheries. We, therefore, eluted stained cells from the scaffolds and applied appropriate gating to collect all the cells of both types while excluding debris (Figs. 9a, b, 10a, b). We then used flow cytometry to quantitatively determine the viability [50] of the live-dead-stained MG-63 and L929 cells seeded on the AM Fe scaffolds and Ti64 controls (Figs. 9 and 10). The cells cultured on the scaffolds in the bioreactor under static and dynamic conditions were compared. In comparison to the static cultures (Figs. 9e and 10e), the fraction of the viable MG-63 and L929 cells cultured dynamically on the Fe scaffolds increased by >14% and >4%, while the respective percentages of the dead cells decreased by >9% and >20%, respectively (Figs. 9f and 10f). On the Ti64 control specimens, the percentage of the viable MG-63 and L929 cells increased from 70.5% to 85.5% and from 61.4% to 87.7%, respectively, when switching from the static (Figs. 9g and 10g) to the dynamic culture condition (Figs. 9h and 10h). For both Fe and Ti64 specimens, the percentages of viable cells under dynamic condition all increased significantly ($p<0.05$) compared with the static ones.

4. Discussion

We compared the biodegradation behavior and cytocompatibility of AM porous Fe scaffolds under semi-physiological static and customized physiomimetic dynamic flow conditions. The dynamic

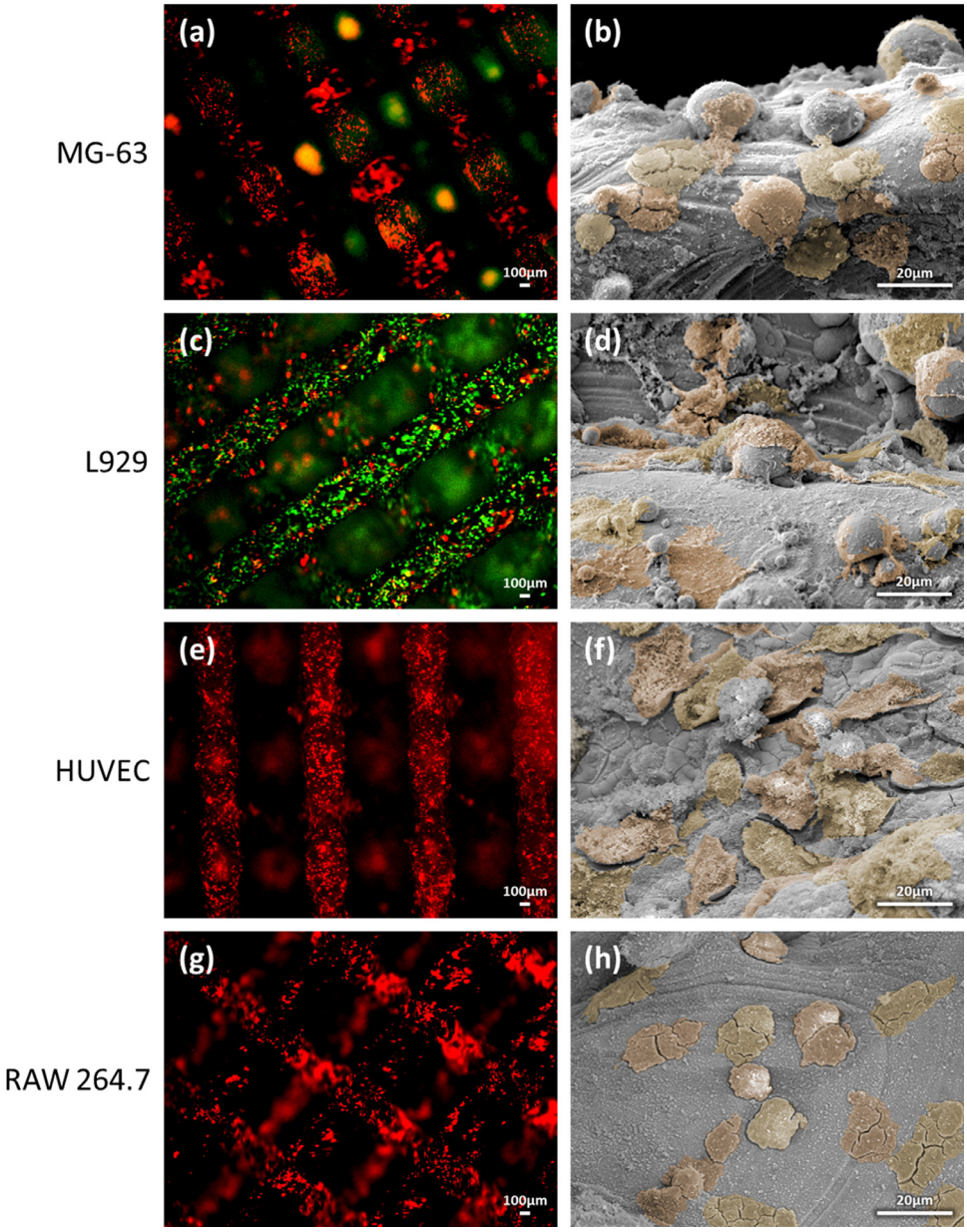

Fig. 7. Biocompatibility of AM porous Fe scaffolds under static *in vitro* conditions. Left panel: fluorescent images of MG-63 (a), L929 (c), HUVEC (e) and RAW 264.7 (g) cells attached to scaffold lattice, 24 h after seeding, with live cells (green) and dead cells (red). Right panel: Scanning electron micrographs showing MG-63 (b), L929 (d), HUVEC (f) and RAW 264.7 (h) cells attached to struts; cells are indicated by yellowish pseudo-coloration for better visualization.

flow conditions are particularly relevant because implanted Fe-based bone substitutes face blood flow [12] and/or interstitial fluid transport [51,52] in the ml/min range in the human body [53].

4.1. Static vs. dynamic biodegradation

To study the *in vitro* biodegradation of the AM Fe scaffolds under physiomimetic conditions, we used the custom-made flow-through bioreactor (Fig. 1) that allowed us to simulate the circulation of body fluid (*e.g.*, using r-SBF) under physiological (*i.e.*, cell culture) conditions. Herewith, we aimed to better comply with the latest recommendations of ISO/TS 37137-1:2021 [54].

Upon implantation, a hydroxide layer is formed on the surface of the AM Fe porous implants, which remains permeable to oxygen. Macroscopic differences in the corrosion layers of our samples suggest the removal of biodegradation products taking place in the fluid flow direction (*i.e.*, the direction of the arrow; Fig. 2), which is reminiscent of *in vivo* excretion. Oxygen may have transformed the ferrous hydroxides of the outer corrosion layer into brownish iron hydroxide, as the most common corrosion product [55]. Also, Fe ions may have formed orange-brownish insoluble degradation products at the biomaterial/tissue interface [56]. This agrees with the EDS results regarding Fe precipitates that mainly contains Fe, O, and C (Fig. 3). The dynamic conditions increased the rates of biodegradation as measured by weight loss and ion release. The actual *in vitro* biodegradation rate in our setup may be even higher, because the cleaning process did not manage to remove all the biodegradation products present on the surface of the specimens (Fig. 4). Our scaffolds lost 8% of their weight within four weeks, which corresponds to a theoretical complete degrada-

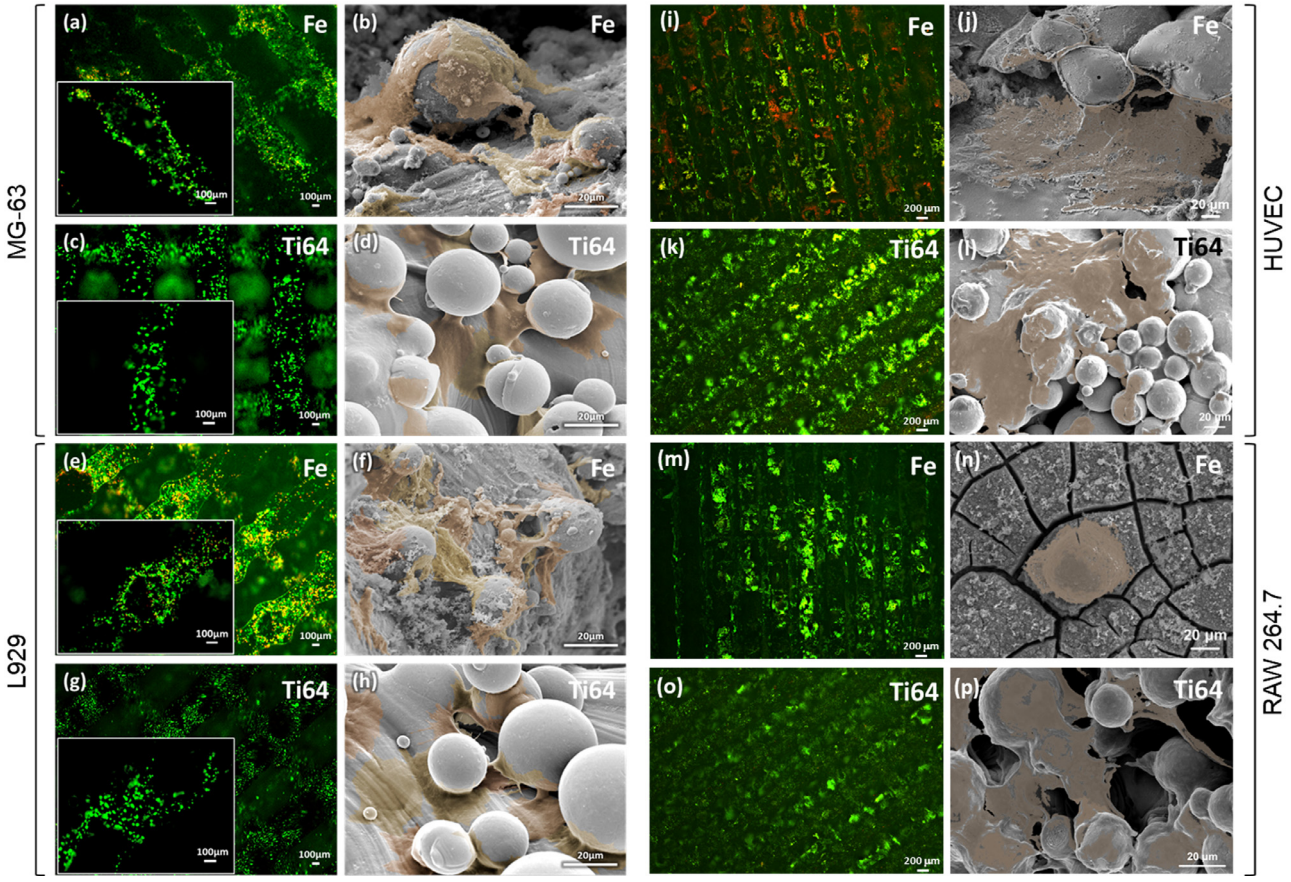

Fig. 8. The biocompatibility of AM porous Fe scaffolds under dynamic *in vitro* conditions: the fluorescent images of the MG-63 (a,), L929 (e,), HUVEC (i), and RAW 264.7 (m) cells, attached to the Fe scaffold lattice; the corresponding images of the same cells on the AM titanium (Ti64) specimens (c, g, k, o), with live (green) and dead (red) cells (24 h after seeding); on the right, the corresponding pseudo-colored scanning electron micrographs of the same cell types on the Fe (b, f, j, n) and Ti64 (d, h, l, p) specimens.

tion rate within 1-2 years. The animal studies available in the literature suggest that the actual *in vivo* rates of biodegradation may be somewhat lower [23,25,57].

The increased ion release under dynamic conditions exacerbates the increase in the osmolarity of the medium, but a hyperosmolarity of 5-20 mOsm/kg (0.30-0.32 osmole/kg) (Fig. 2) is unlikely to be detrimental to most skeletal cell types [58,59]. Such a 5-fold increase in the concentration of the Fe ion under the dynamic conditions, as compared to the static ones, is expected to be tolerated by the cells as long as they are not internalized. For the L929 cells, the internalization of Fe requires >3 mM of (artificially added) extracellular ions, which may then induce pH changes of 0.4-0.5 units [60]. In our experiments, the biodegradation of the AM porous Fe between days 7 and 28 caused a weight loss of 231 mg (Fig. 2) with ion concentrations ranging between 17.9 µM and 71-90 µM under static and dynamic conditions, respectively. These values are all sub millimolar. Moreover, while relative pH changes in both of our conditions were almost identical (Fig. 2), an absolute maximal shift of about 0.2 units from the starting pH occurred. Osteoblasts and other cell types respond to changes as little as 0.1 pH unit [61–64]. This might affect the mitochondrial activity and potentially influence some (MTT-based) cytotoxicity assays. Dynamic biodegradation conditions under which the surface of the specimens is constantly washed by medium may inhibit local pitting [65]. Moreover, even in the event of full degradation of a 10 gram Fe implant in an adult person, the systemic serum iron concentration would not exceed safe values, assuming a conservative blood volume of about 2,800 ml and a high baseline of Fe-load of 447 mg/l in blood [66]. However, cytotoxicity is not solely a function of released (soluble) ions, but also a function of the insoluble degradation products at the biomaterial/cell interface [56].

4.2. Cell type-dependent biocompatibility

A bone fracture hematoma represents a complex cellular environment, involving inflammation, cellular migration, and proliferation to restore tissue integrity [67]. Therefore, we studied, for the first time, the cytocompatibility of pure Fe using four cell types. We chose murine macrophages (RAW264.7) as a cell type of the innate immune response, fibroblasts (L929) to represent the integument due to their similarity to human dermal fibroblasts [68], human endothelial cells (HUVEC) as an established model to study angiogenic responses *in vitro* [69,70], and human MG-63 cells as anabolic bone cells [71]. The latter are well characterized [72,73], and were also used in our earlier study [74] and in combination with different biomaterials, particularly Fe-based alloys [75–77].

The quantification of live and dead cells on, and particularly inside of, 3D (porous) metal scaffolds is challenging due to strut opacity. We, thus, initially analyzed the cell seeding efficacies associated with our specimens (Fig. 5) to get a first impression of their cytocompatibility. No significant differences between our four cell types were found. This is in contrast with the studies reporting a selective adhesion advantage of osteoblast-like MG-63 cells over L929 fibroblasts [78]. However, our conditions were different

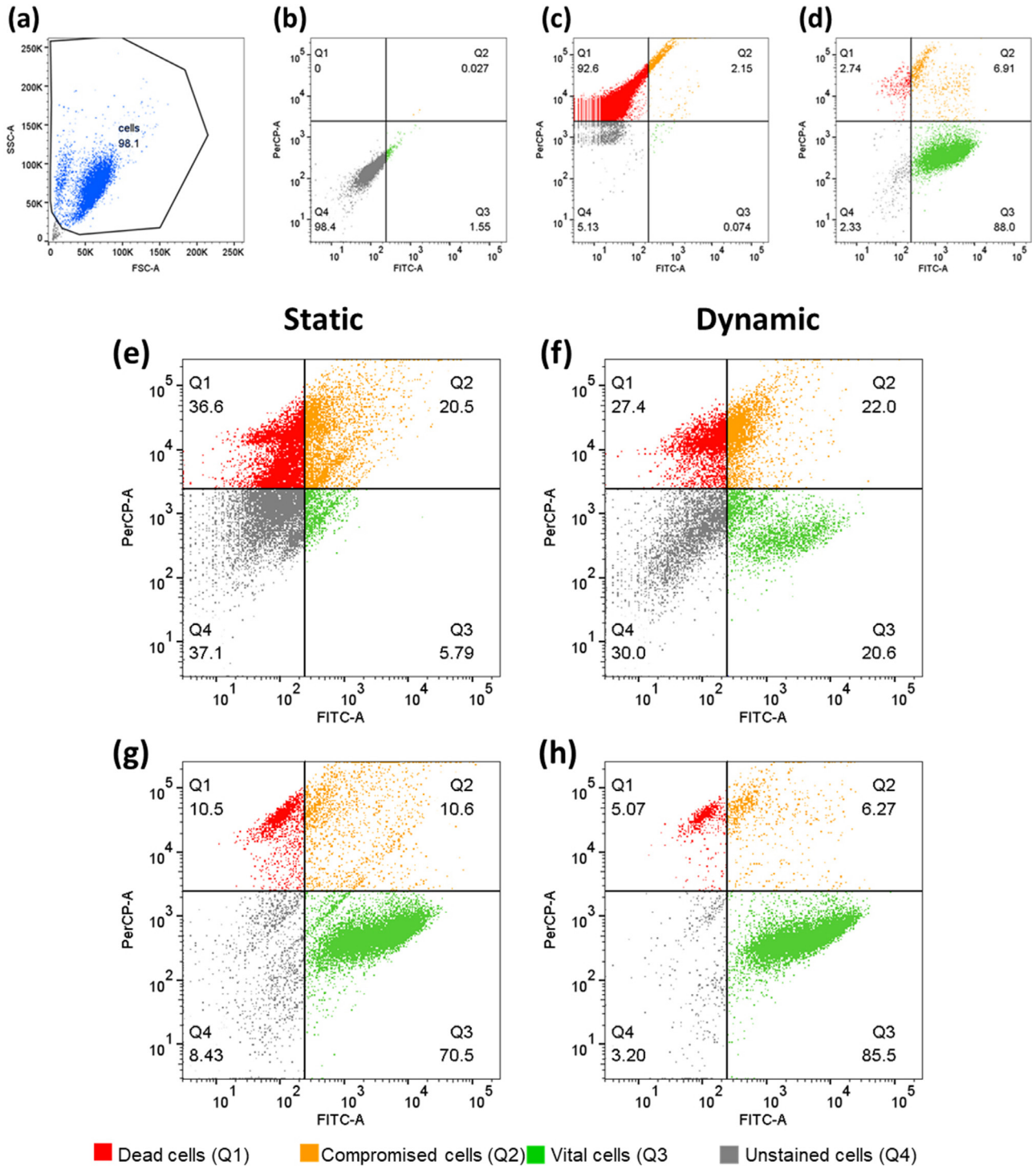

Fig. 9. The comparative flow cytometric cell viability of the MG-63 cells after 24 h of direct contact with the AM porous scaffolds under static (e, g) and dynamic (f, h) *in vitro* conditions. The quantitative analyses of the live-dead stained cells on the Fe (e, f) and Ti64 (g, h) specimens, respectively. The cell gating of the excluded debris (a), unstained cell population (b), lysed cells after staining (c), and normal cells after staining (d).

from those of the previous study. Many factors, including cell type, cell density, scaffold type, scaffold geometry, and scaffold chemistry, can affect biocompatibility [79], and we next looked into cell type differences in more detail.

Indirect extract-based cytotoxicity assays showed that, at day 28, the concentration of the Fe ion reaches 4.6 mg/l under dynamic conditions (Fig. 2), which equals 1.35 mg of released Fe per 300 ml of medium. Statically, ≈1 mg/l or ≈17.9 µM of Fe is constantly released over 28 days. In contrast, under dynamic conditions about 71 µM (day 7 onwards) to 90 µM (day 28) Fe ions were dynamically released. It has been shown that up to 900 µM (*i.e.*, 50 µg/ml) of artificially added Fe ions does not cause immediate cytotoxic effects on human endothelial cells [80]. This is not surprising, given that a typical adult human contains 3–5 g of Fe [81,82], mostly in the bone marrow [81,82]. Furthermore, the bioavailability of Fe is relatively limited under physiological aerobic conditions. That is because soluble Fe(II) (heme) readily oxidizes to Fe(III) (non-heme iron), which is virtually insoluble [12,56]. In-

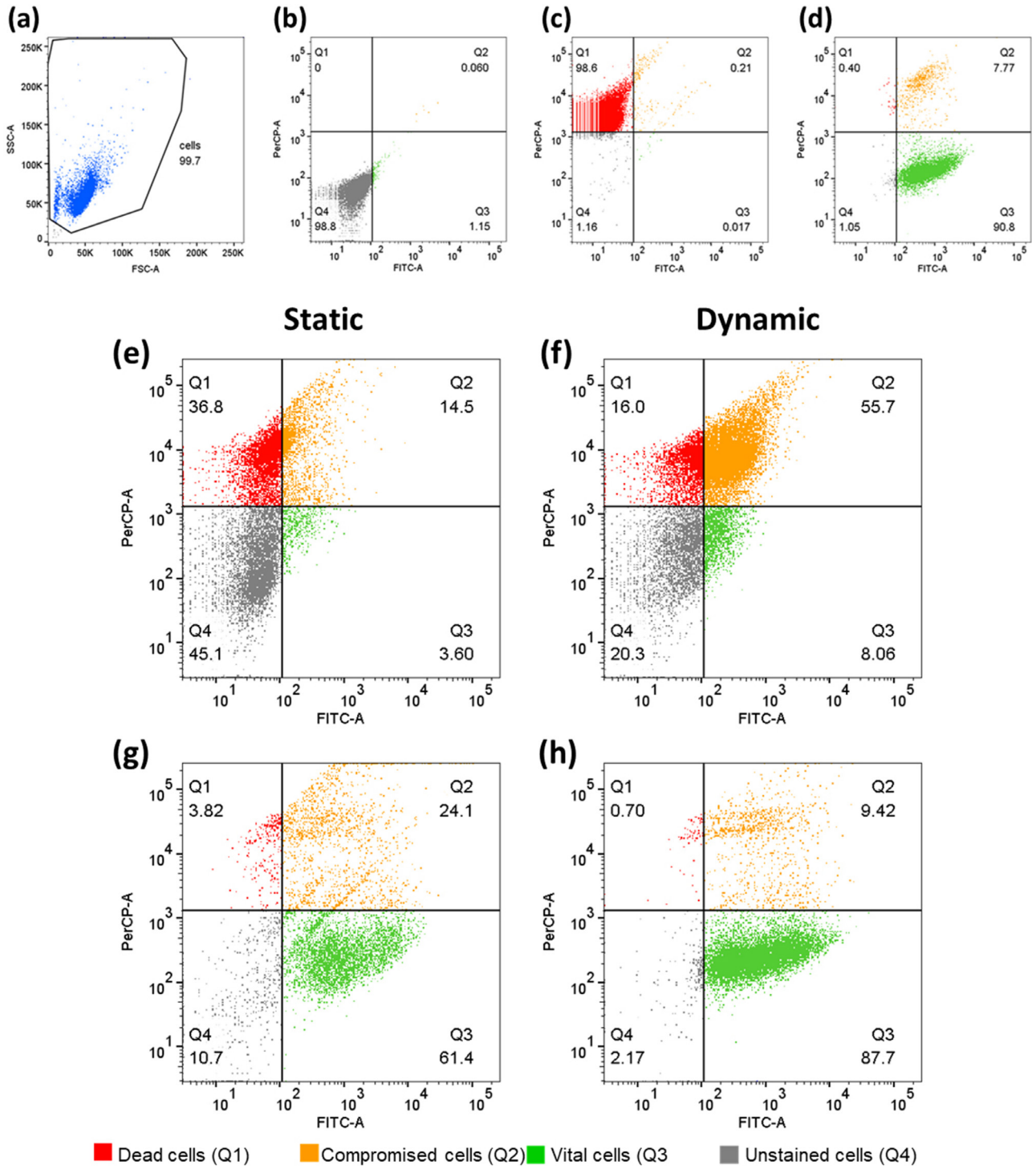

Fig. 10. A comparative flow cytometric cell viability of the L929 cells after 24 h of direct contact with the AM porous scaffolds under static (e, g) and dynamic (f, h) *in vitro* conditions. The quantitative analyses of the live-dead stained cells on the Fe (e, f) and Ti64 (g, h) specimens, respectively. The cell gating of the excluded debris (a), unstained cell population (b), lysed cells after staining (c), and normal cells after staining (d).

deed, the cytotoxicity of L929 cells may have been caused by the size of the corrosion products, but not the Fe itself [60], suggesting that supernatants and biodegradation products should be assessed separately in the future. Particles size-mediated cytotoxicity also highlights the potentially important role of phagocytosing macrophages, which were represented by RAW 264.7 cells in our experiments.

The available ISO standards set the cytotoxicity thresholds at 30% of the *standard-of-care*, based on which biodegradable Fe stents have been earlier assessed to be cytocompatible [83]. Using Ti64 scaffolds as the positive control, we confirmed that the L929 cells never (up to 72 h) reveal a cytotoxic response to the extracts of our scaffolds. In contrast, all other cell types showed a significantly reduced mitochondrial activity in MTS-based assays upon long-term incubation. Cell type-dependent cytotoxicity differences are reported in other fields, which are in agreement with our earlier data [84,85]. A reason for this cell type-specific behavior may be that the doubling times of cell populations differ between cell

lines. For instance, RAW 264.7 cells were reported to have a much shorter doubling time than L929 cells [86], which may influence the interpretation of cytocompatibility data obtained from the tests with different cell lines [87]. On the other hand, L929 cells may be more sensitive to stressors than other cell types on modified Ti64 surfaces [88]. Although it is well accepted that test conditions can affect the *in vitro* cytotoxicity results of biodegradable metallic biomaterials [35], surprisingly few investigators drew conclusions regarding the *in vitro* toxicity of Fe based on indirect contact results from more than a single cell type.

While Fe is essential for many biological processes, it also poses a biological hazard as it may generate reactive organic species (ROS) through Fenton chemistry [81,82] to cause "oxidative stress" and inflammatory responses that impact the musculoskeletal system [89,90]. Some cell damage caused by corrosion-mediated ROS production may, therefore, be unavoidable, despite effective cellular anti-oxidant defense systems *in vivo* [91]. While indirect assays are often preferred due to their ease of quantification [92–94] and may make it possible to isolate the effects of biodegradation products, they will likely not capture the effects of short-lived ROS.

In indirect contact assays, the material is firstly immersed in a extraction vehicle (*e.g.*, culture medium) under physiological conditions (*e.g.*, 24-72 h/37°C) [66]. It, however, remains unclear whether the observed degrees of cytotoxicity are a response to (1) the concentration of the released ions, (2) a consequence of the physical contact between cells and the metal, or (3) a combination of both [95]. To better mimic *in vivo* situations *in vitro*, we applied the suggested modifications to EN ISO 10993-5 and 10993-12, such as using a 10-times higher extraction ratio [33,34]. However, for AM porous iron, a 10-times dilution ratio may be even insufficient. Compared to solid disk-shaped specimens, AM porous biodegradable metals have much larger surface area, *e.g.*, 27 cm^2 for the AM porous iron in this work. According to the findings of our previous study, the degradation rate increased with increasing porosity, which could lead to a higher Fe ion concentration and a higher local pH value near the scaffolds [20]. The higher Fe ion concentration can promote the formation of ROS that are toxic due to their ability of rapid reaction with most molecules in living cell. Thus, AM porous iron may exhibit lower compatibility than its solid counterpart *in vitro*, although the *in vivo* results may be different.

For all the cell types, the results of the indirect extract-based cytotoxicity assays were more promising than those obtained using direct contact assessment under static conditions (at 24 h). In line with ISO recommendations, our Fe extracts were prepared by incubating AM Fe scaffolds for up to 72 h in the cell culture medium under physiological conditions, which is harsh. Extract-treated cells then showed the results that contradicted those reported by several other studies in which shorter evaluation times of 24-48 h were used [96]. As compared to the MG-63 cells, the L929 fibroblasts exhibited a high degree of compatibility with the AM porous iron specimens even under unfavorable static culture conditions and with 72 h extracts, performing similar to Ti64 controls. For the biomaterials that have a close, long-term contact with tissues, it is necessary to perform direct contact biocompatibility assessment [97]. Importantly though, our results suggest that only the direct contact between Fe and cells, but not the degradation products, causes cytotoxicity and oxidative stress [98]. Carefully designed experiments controlling for all relevant covariates are, however, required for a more decisive conclusion.

Direct contact cytocompatibility assessment is more difficult on bulk materials, such as (porous) metals, due to a limited visibility of cells. First, we combined SEM analyses with semi-quantitative staining to differentially label live and dead cells simultaneously with two fluorescent dyes: a membrane permeant non-fluorescent dye (Calcein-AM) depending on active metabolism to render green fluorescent was used to indicate living cells, while cell impermeable and red fluorescent intercalating dye propidium iodide (PI) was used as indicator of dead cells with compromised plasma membranes. Under static culture conditions, SEM analyses showed rounded morphology for the MG-63, RAW 264.7, and HUVEC cells after 24 h of contact with the specimens. Although visual classification of cell death remains challenging, these condensations may be indicative of apoptosis [99,100]. Furthermore, SEM revealed that the cells were covered by the fine dust of the biodegradation particles, which may increase local toxicity [101]. As our dynamic culture conditions mimics the *in vivo* situation, cell morphology and cell viability improvements were observed. Similar to Ti64, the majority of the MG-63 and L929 cells presented a green fluorescence signal, enhanced cell-material and cell-cell contact, and filopodial projections. In contrast to the static culture conditions, a dynamic cell culture increases cell viability because of a constant supply of fresh medium and the removal of potentially toxic biodegradation products [101,102]. The limited solubility of iron is both a challenge and an advantage, since it limits its toxicity [81]. Our study reveals a cellular activity >75% within the first 24 h of contact with Fe extracts followed by a decline thereafter, which highlights the importance of using multiple time points to better understand the long-term effects of such biodegradable biomaterials. Finally, it is important to acknowledge the limitations of direct-contact assays, because it is not always clear if they provide information regarding cell attachment, proliferation, or cytotoxicity [66].

The contribution of this study is the combination of live-dead staining with flow cytometrical analyses to quantify cell viability with increase speed and accuracy. While using flow cytometry to improve the study of cytotoxicity has been reported before [50,103], it has been hardly applied in biomaterial research. This technique allows for combining semi-quantitative visual inspection of green and red cells with quantification upon subsequent release of the cells from the specimens. With an excitation range between 400 and 600 nm, and emitting light between 600 and 700 nm, PI can be combined with Calcein-AM [50], PI/Per-CP (Y-axis), and Calcein-AM/FITC (X-axis) using blue laser excitation with distinguishable emission spectra (*i.e.*, 525 nm and 670 nm, respectively).

On Fe struts, the dynamic culture conditions resulted in 2.5 times more vital MG-63 cells (Q3) than under the static conditions. Under the same conditions, the dynamic culture conditions increased the viability of the MG-63 cells by 22% even on Ti64. The dynamic culture conditions also improved the viability of L929 by 2.2 times and 41% times on Fe and Ti64, respectively. In contrast to the semi-quantitative counting of green *versus* red cells which is only possible on the peripheral surfaces of the specimens, flow cytometry ensures a much higher accuracy by counting thousands of cells simultaneously. However, PI cannot detect dying cells or distinguish between the different types of cell death. Even Calcein-AM is incapable of detecting very early apoptotic cells [50], which is why the procedure may benefit from co-staining with Annexin V. High Fe ion release (> 3mM) may result in intracellular Fe accumulation, which may quench Calcein fluorescence [104,105]. Quenching phenomena might have affected the Q2 gating, while potential PI leakage could have influenced the Q3 signals [106].

This study demonstrated the importance of cell type selection and setting up a standard for *in vitro* testing of future (biodegradable) medical devices in general and Fe-based scaffolds in particular. Bioreactors have been used to reproduce the microenvironment of stents more faithfully [107], but still suffer from the absence of plasma clearance [66]. Importantly, biocompatibility is even more complex to define *in vivo* than *in vitro*. Future *in vitro* models that can appropriately mimic the human blood (*i.e.*, r-SBF with serum) to account for high-affinity Fe-binding proteins may improve the predictive power of such *in vitro* techniques [56].

5. Conclusions

We studied the cytocompatibility of AM biodegradable porous iron using multiple cell lines under both static and dynamic culture conditions. Our results show a highly cell type-specific tolerance level for such biodegradable metallic scaffolds, suggesting that the results from single cell type-based assays should be interpreted with caution. In general, L929 cells appeared overall more robust in indirect and direct assays than the MG-63, RAW 264.7 and HUVEC cells, especially with prolonged incubation times. Moreover, we found large difference between the results corresponding to static culture conditions and those obtained under dynamic culture conditions that aim to better simulate the *in vivo* conditions. All assays consistently showed an improved tolerability under physiomimetic dynamic fluid flow conditions as compared to the traditional static cultures. The results of this study have implications for future *in vitro* cytocompatibility analyses of other (AM porous) biodegradable biomaterials. Such improvements would mean that smaller number of *in vivo* experiments need to be performed. Overall, this study challenges the current *status quo* regarding the biological risk evaluation of biodegradable metals and highlights the importance of using dynamic physiomimetic conditions and multiple cell types for such types of experiments. Moreover, this study shows, for the first time, that ISO/TS 37137-1:2021 is superior to ISO 10993 standards [66] for the biological evaluation of degradable Fe-based biomaterials.

Declaration of Competing Interest

The authors declare that they have no known competing financial interests or personal relationships that could have appeared to influence the work reported in this paper.

Acknowledgements

We gratefully acknowledge financial support from the Interreg Flanders – The Netherlands program (CCI Grant No. 2014TC16RFCB04), the START program of the Medical Faculty of the RWTH Aachen University (grant No. 133/20), the Interdisciplinary Centre for Clinical Research (IZKF) of the Faculty of Medicine of the RWTH Aachen University (OC1-1), and the START Initiative for targeted research funding at the Medical Faculty of RWTH Aachen University. Y. Li also thanks the financial support from the National Natural Science Foundation of China (52201294), China Postdoctoral Science Foundation (2022M710345), Natural Science Foundation of Beijing (L212014), and Fundamental Research Funds for the Central Universities and the Youth Teacher International Exchange & Growth Program (No. QNXM20220022).

References

[1] G.L. Koons, M. Diba, A.G. Mikos, Materials design for bone-tissue engineering, Nat. Rev. Mater. 5 (8) (2020) 584–603.
[2] A.A. Zadpoor, Mechanical performance of additively manufactured meta-biomaterials, Acta Biomater. 85 (2019) 41–59.
[3] E. Davoodi, H. Montazerian, A.S. Mirhakimi, M. Zhianmanesh, O. Ibhadode, S.I. Shahabad, R. Esmaeilizadeh, E. Sarikhani, S. Toorandaz, S.A. Sarabi, R. Nasiri, Y. Zhu, J. Kadkhodapour, B. Li, A. Khademhosseini, E. Toyserkani, Additively manufactured metallic biomaterials, Bioact. Mater. (2021).
[4] T. Zhang, Q. Wei, H. Zhou, Z. Jing, X. Liu, Y. Zheng, H. Cai, F. Wei, L. Jiang, M. Yu, Y. Cheng, D. Fan, W. Zhou, X. Lin, H. Leng, J. Li, X. Li, C. Wang, Y. Tian, Z. Liu, Three-dimensional-printed individualized porous implants: a new "implant-bone" interface fusion concept for large bone defect treatment, Bioact. Mater. 6 (11) (2021) 3659–3670.
[5] M. Lowther, S. Louth, A. Davey, A. Hussain, P. Ginestra, L. Carter, N. Eisenstein, L. Grover, S. Cox, Clinical, industrial, and research perspectives on powder bed fusion additively manufactured metal implants, Addit. Manuf. 28 (2019) 565–584.
[6] X. Liu, Z. Yue, T. Romeo, J. Weber, T. Scheuermann, S. Moulton, G. Wallace, Biofunctionalized anti-corrosive silane coatings for magnesium alloys, Acta Biomater. 9 (10) (2013) 8671–8677.
[7] T.H. Lin, Y. Tamaki, J. Pajarinen, H.A. Waters, D.K. Woo, Z. Yao, S.B. Goodman, Chronic inflammation in biomaterial-induced periprosthetic osteolysis: NF-κB as a therapeutic target, Acta Biomater. 10 (1) (2014) 1–10.
[8] S.M. Skovdal, N.P. Jørgensen, E. Petersen, S. Jensen-Fangel, R. Ogaki, G. Zeng, M.I. Johansen, M. Wang, H. Rohde, R.L. Meyer, Ultra-dense polymer brush coating reduces Staphylococcus epidermidis biofilms on medical implants and improves antibiotic treatment outcome, Acta Biomater. 76 (2018) 46–55.
[9] X. Gao, Z. Xu, G. Liu, J. Wu, Polyphenols as a versatile component in tissue engineering, Acta Biomater. 119 (2021) 57–74.
[10] Y. Li, H. Jahr, J. Zhou, A.A. Zadpoor, Additively manufactured biodegradable porous metals, Acta Biomater. 115 (2020) 29–50.
[11] J. Zhang, Y. Jiang, Z. Shang, B. Zhao, M. Jiao, W. Liu, M. Cheng, B. Zhai, Y. Guo, B. Liu, X. Shi, B. Ma, Biodegradable metals for bone defect repair: a systematic review and meta-analysis based on animal studies, Bioact. Mater. 6 (11) (2021) 4027–4052.
[12] G. Gąsior, J. Szczepański, A. Radtke, Biodegradable iron-based materials-what was done and what more can Be done? Materials 14 (12) (2021).
[13] Y. Li, H. Jahr, K. Lietaert, P. Pavanram, A. Yilmaz, L.I. Fockaert, M.A. Leeflang, B. Pouran, Y. Gonzalez-Garcia, H. Weinans, J.M.C. Mol, J. Zhou, A.A. Zadpoor, Additively manufactured biodegradable porous iron, Acta Biomater. 77 (2018) 380–393.
[14] Y. Li, J. Zhou, P. Pavanram, M.A. Leeflang, L.I. Fockaert, B. Pouran, N. Tümer, K.U. Schröder, J.M.C. Mol, H. Weinans, H. Jahr, A.A. Zadpoor, Additively manufactured biodegradable porous magnesium, Acta Biomater. 67 (2018) 378–392.
[15] Y. Li, P. Pavanram, J. Zhou, K. Lietaert, P. Taheri, W. Li, H. San, M.A. Leeflang, J.M.C. Mol, H. Jahr, A.A. Zadpoor, Additively manufactured biodegradable porous zinc, Acta Biomater. 101 (2020) 609–623.
[16] B. Liu, Y.F. Zheng, Effects of alloying elements (Mn, Co, Al, W, Sn, B, C and S) on biodegradability and in vitro biocompatibility of pure iron, in: Acta Biomater., 7, 2011, pp. 1407–1420.
[17] R. Gorejová, L. Haverová, R. Oriňaková, A. Oriňak, M. Oriňak, Recent advancements in Fe-based biodegradable materials for bone repair, J. Mater. Sci. 54 (3) (2019) 1913–1947.
[18] Y. Nie, G. Chen, H. Peng, S. Tang, Z. Zhou, F. Pei, B. Shen, In vitro and 48 weeks in vivo performances of 3D printed porous Fe-30Mn biodegradable scaffolds, Acta Biomater. 121 (2021) 724–740.
[19] N.E. Putra, M.A. Leeflang, M. Minneboo, P. Taheri, L.E. Fratila-Apachitei, J.M.C. Mol, J. Zhou, A.A. Zadpoor, Extrusion-based 3D printed biodegradable porous iron, Acta Biomater. 121 (2021) 741–756.
[20] Y. Li, H. Jahr, P. Pavanram, F.S.L. Bobbert, U. Puggi, X.Y. Zhang, B. Pouran, M.A. Leeflang, H. Weinans, J. Zhou, A.A. Zadpoor, Additively manufactured functionally graded biodegradable porous iron, Acta Biomater. 96 (2019) 646–661.
[21] Y. Li, K. Lietaert, W. Li, X.Y. Zhang, M.A. Leeflang, J. Zhou, A.A. Zadpoor, Corrosion fatigue behavior of additively manufactured biodegradable porous iron, Corros. Sci. 156 (2019) 106–116.
[22] A. Francis, Y. Yang, S. Virtanen, A.R. Boccaccini, Iron and iron-based alloys for temporary cardiovascular applications, J. Mater. Sci. 26 (3) (2015) 1–16.
[23] M. Peuster, C. Hesse, T. Schloo, C. Fink, P. Beerbaum, C. von Schnakenburg, Long-term biocompatibility of a corrodible peripheral iron stent in the porcine descending aorta, Biomaterials 27 (28) (2006) 4955–4962.
[24] M. Peuster, P. Wohlsein, M. Brügmann, M. Ehlerding, K. Seidler, C. Fink, H. Brauer, A. Fischer, G. Hausdorf, A novel approach to temporary stenting: degradable cardiovascular stents produced from corrodible metal—results 6–18 months after implantation into New Zealand white rabbits, Heart 86 (5) (2001) 563–569.
[25] T. Kraus, F. Moszner, S. Fischerauer, M. Fiedler, E. Martinelli, J. Eichler, F. Witte, E. Willbold, M. Schinhammer, M. Meischel, P.J. Uggowitzer, J.F. Löffler, A. Weinberg, Biodegradable Fe-based alloys for use in osteosynthesis: outcome of an in vivo study after 52weeks, Acta Biomater. 10 (7) (2014) 3346–3353.
[26] C. Yang, Z. Huan, X. Wang, C. Wu, J. Chang, 3D printed Fe scaffolds with HA nanocoating for bone regeneration, ACS Biomater. Sci. Eng. 4 (2) (2018) 608–616.
[27] R. Oriňáková, A. Oriňák, L.M. Bučková, M. Giretová, Ľ. Medvecký, E. Labbanczová, M. Kupková, M. Hrubovčáková, K. Kovaľ, Iron based degradable foam structures for potential orthopedic applications, Int. J. Electrochem. Sci. 8 (2013) 12451–12465.
[28] D.-T. Chou, D. Wells, D. Hong, B. Lee, H. Kuhn, P.N. Kumta, Novel processing of iron–manganese alloy-based biomaterials by inkjet 3-D printing, Acta Biomater. 9 (10) (2013) 8593–8603.
[29] D. Andreas, H. Thomas, B.F. Wilhelm, P. Matthias, In vitro and in vivo corrosion properties of new iron–manganese alloys designed for cardiovascular applications, J. Biomed. Mater. Res. B 103 (3) (2015) 649–660.
[30] R.H. Stewart, A modern view of the interstitial space in health and disease, Front. Vet. Sci. 7 (2020) 609583.
[31] A.H.M. Sanchez, B.J.C. Luthringer, F. Feyerabend, R. Willumeit, Mg and Mg alloys: how comparable are in vitro and in vivo corrosion rates? A review, Acta Biomater. 13 (2015) 16–31.
[32] U.T. Seyfert, V. Biehl, J. Schenk, In vitro hemocompatibility testing of biomaterials according to the ISO 10993-4, Biomol. Eng. 19 (2) (2002) 91–96.
[33] J. Fischer, D. Pröfrock, N. Hort, R. Willumeit, F. Feyerabend, Reprint of: improved cytotoxicity testing of magnesium materials, Mater. Sci. Eng., B 176 (20) (2011) 1773–1777.

[34] J. Wang, F. Witte, T. Xi, Y. Zheng, K. Yang, Y. Yang, D. Zhao, J. Meng, Y. Li, W. Li, K. Chan, L. Qin, Recommendation for modifying current cytotoxicity testing standards for biodegradable magnesium-based materials, Acta Biomater. 21 (2015) 237–249.
[35] E. Jablonská, J. Kubásek, D. Vojtěch, T. Ruml, J. Lipov, Test conditions can significantly affect the results of in vitro cytotoxicity testing of degradable metallic biomaterials, Sci. Rep. 11 (1) (2021) 6628.
[36] H. Hermawan, Updates on the research and development of absorbable metals for biomedical applications, Prog. Biomater. 7 (2) (2018) 93–110.
[37] D. Dunning, Basic mammalian bone anatomy and healing, Vet Clin. North Am. Exot. Anim. Pract. 5 (1) (2002) 115–128.
[38] J. Zhou, Y. Yang, M.Alonso Frank, R. Detsch, A.R. Boccaccini, S. Virtanen, Accelerated degradation behavior and cytocompatibility of pure iron treated with sandblasting, ACS Appl. Mater. Interfaces 8 (40) (2016) 26482–26492.
[39] J. Markhoff, M. Krogull, C. Schulze, C. Rotsch, S. Hunger, R. Bader, Biocompatibility and inflammatory potential of titanium alloys cultivated with human osteoblasts, fibroblasts and macrophages, Materials 10 (1) (2017) 52.
[40] J.M. Anderson, Future challenges in the in vitro and in vivo evaluation of biomaterial biocompatibility, Regen. Biomater. 3 (2) (2016) 73–77.
[41] C.S. Bahney, R.L. Zondervan, P. Allison, A. Theologis, J.W. Ashley, J. Ahn, T. Miclau, R.S. Marcucio, K.D. Hankenson, Cellular biology of fracture healing, J. Orthop. Res. 37 (1) (2019) 35–50.
[42] V.I. Sikavitsas, G.N. Bancroft, H.L. Holtorf, J.A. Jansen, A.G. Mikos, Mineralized matrix deposition by marrow stromal osteoblasts in 3D perfusion culture increases with increasing fluid shear forces, PNAS 100 (25) (2003) 14683–14688.
[43] P.-h.G. Chao, W. Grayson, G. Vunjak-Novakovic, Engineering cartilage and bone using human mesenchymal stem cells, J. Orthop. Sci. 12 (4) (2007) 398.
[44] A. Oyane, H.-M. Kim, T. Furuya, T. Kokubo, T. Miyazaki, T. Nakamura, Preparation and assessment of revised simulated body fluids, J. Biomed. Mater. Res. A 65A (2) (2003) 188–195.
[45] F. Zhao, B. van Rietbergen, K. Ito, S. Hofmann, Flow rates in perfusion bioreactors to maximise mineralisation in bone tissue engineering in vitro, J. Biomech. 79 (2018) 232–237.
[46] J.R. Vetsch, D.C. Betts, R. Müller, S. Hofmann, Flow velocity-driven differentiation of human mesenchymal stromal cells in silk fibroin scaffolds: a combined experimental and computational approach, PLoS One 12 (7) (2017) e0180781.
[47] J.M. Sobral, S.G. Caridade, R.A. Sousa, J.F. Mano, R.L. Reis, Three-dimensional plotted scaffolds with controlled pore size gradients: effect of scaffold geometry on mechanical performance and cell seeding efficiency, Acta Biomater. 7 (3) (2011) 1009–1018.
[48] K. Shimizu, A. Ito, H. Honda, Enhanced cell-seeding into 3D porous scaffolds by use of magnetite nanoparticles, J. Biomed. Mater. Res. B 77B (2) (2006) 265–272.
[49] S. Barui, A.K. Panda, S. Naskar, R. Kuppuraj, S. Basu, B. Basu, 3D inkjet printing of biomaterials with strength reliability and cytocompatibility: quantitative process strategy for Ti-6Al-4V, Biomaterials 213 (2019) 119212.
[50] L.C. Crowley, A.P. Scott, B.J. Marfell, J.A. Boughaba, G. Chojnowski, N.J. Waterhouse, Measuring cell death by propidium iodide uptake and flow cytometry, Cold Spring Harb. Protoc. (7) (2016) 2016.
[51] H. Wiig, M.A. Swartz, Interstitial fluid and lymph formation and transport: physiological regulation and roles in inflammation and cancer, Physiol. Rev. 92 (3) (2012) 1005–1060.
[52] M.A. Swartz, A. Kaipainen, P.A. Netti, C. Brekken, Y. Boucher, A.J. Grodzinsky, R.K. Jain, Mechanics of interstitial-lymphatic fluid transport: theoretical foundation and experimental validation, J. Biomech. 32 (12) (1999) 1297–1307.
[53] A.P. Md. Saad, N. Jasmawati, M.N. Harun, M.R. Abdul Kadir, H. Nur, H. Hermawan, A. Syahrom, Dynamic degradation of porous magnesium under a simulated environment of human cancellous bone, Corros. Sci. 112 (2016) 495–506.
[54] I. TS, Biological evaluation of absorbable medical devices — Part 1: General requirements, the International Organization for Standardization, ISO/TS 37137-1:2021(en), Biological evaluation of absorbable medical devices — Part 1: General requirements, 2021, pp. 1-99.
[55] M.A. Blesa, E. Matijević, Phase transformations of iron oxides, oxohydroxides, and hydrous oxides in aqueous media, Adv. Colloid Interface Sci. 29 (3) (1989) 173–221.
[56] N.S. Fagali, C.A. Grillo, S. Puntarulo, M.A. Fernández Lorenzo de Mele, Cytotoxicity of corrosion products of degradable Fe-based stents: relevance of pH and insoluble products, Colloids Surf. B 128 (2015) 480–488.
[57] W. Lin, L. Qin, H. Qi, D. Zhang, G. Zhang, R. Gao, H. Qiu, Y. Xia, P. Cao, X. Wang, W. Zheng, Long-term in vivo corrosion behavior, biocompatibility and bioresorption mechanism of a bioresorbable nitrided iron scaffold, Acta Biomater. 54 (Supplement C) (2017) 454–468.
[58] M.M. Caron, A.E. van der Windt, P.J. Emans, L.W. van Rhijn, H. Jahr, T.J. Welting, Osmolarity determines the in vitro chondrogenic differentiation capacity of progenitor cells via nuclear factor of activated T-cells 5, Bone 53 (1) (2013) 94–102.
[59] A.E. van der Windt, E. Haak, R.H. Das, N. Kops, T.J. Welting, M.M. Caron, N.P. van Til, J.A. Verhaar, H. Weinans, H. Jahr, Physiological tonicity improves human chondrogenic marker expression through nuclear factor of activated T-cells 5 in vitro, Arthritis Res. Ther. 12 (3) (2010) R100.
[60] W. Lin, G. Zhang, P. Cao, D. Zhang, Y. Zheng, R. Wu, L. Qin, G. Wang, T. Wen, Cytotoxicity and its test methodology for a bioabsorbable nitrided iron stent, J. Biomed. Mater. Res. B 103 (4) (2015) 764–776.
[61] H. Jahr, M. van Driel, G.J. van Osch, H. Weinans, J.P. van Leeuwen, Identification of acid-sensing ion channels in bone, Biochem. Biophys. Res. Commun. 337 (1) (2005) 349–354.
[62] F.Erra Díaz, E. Dantas, J. Geffner, Unravelling the interplay between extracellular acidosis and immune cells, Mediators Inflamm. 2018 (2018) 1218297.
[63] Z. Zhang, Q. Lai, Y. Li, C. Xu, X. Tang, J. Ci, S. Sun, B. Xu, Acidic pH environment induces autophagy in osteoblasts, Sci. Rep. 7 (2017) 46161.
[64] T.R. Arnett, Extracellular pH regulates bone cell function, J. Nutr. 138 (2) (2008) 415S–418S.
[65] J. Lévesque, H. Hermawan, D. Dubé, D. Mantovani, Design of a pseudo-physiological test bench specific to the development of biodegradable metallic biomaterials, Acta Biomater. 4 (2) (2008) 284–295.
[66] E. Scarcello, D. Lison, Are Fe-based stenting materials biocompatible? A critical review of of in vitro and in vivo studies, J. Funct .Biomater. 11 (1) (2019).
[67] K. Schmidt-Bleek, H. Schell, P. Kolar, M. Pfaff, C. Perka, F. Buttgereit, G. Duda, J. Lienau, Cellular composition of the initial fracture hematoma compared to a muscle hematoma: a study in sheep, J. Orthop. Res. 27 (9) (2009) 1147–1151.
[68] R. Chen, A.M. Salisbury, S.L. Percival, In vitro cellular viability studies on a concentrated surfactant-based wound dressing, Int. Wound J. 16 (3) (2019) 703–712.
[69] Z. Chen, A. Htay, W. Dos Santos, G.T. Gillies, H.L. Fillmore, M.M. Sholley, W.C. Broaddus, In vitro angiogenesis by human umbilical vein endothelial cells (HUVEC) induced by three-dimensional co-culture with glioblastoma cells, J. Neurooncol. 92 (2) (2009) 121–128.
[70] H. Yukawa, K. Suzuki, K. Aoki, T. Arimoto, T. Yasui, N. Kaji, T. Ishikawa, T. Ochiya, Y. Baba, Imaging of angiogenesis of human umbilical vein endothelial cells by uptake of exosomes secreted from hepatocellular carcinoma cells, Sci. Rep. 8 (1) (2018) 6765.
[71] A. Billiau, V.G. Edy, H. Heremans, J. Van Damme, J. Desmyter, J.A. Georgiades, P. De Somer, Human interferon: mass production in a newly established cell line, MG-63, Antimicrob. Agents Chemother. 12 (1) (1977) 11–15.
[72] C. Pautke, M. Schieker, T. Tischer, A. Kolk, P. Neth, W. Mutschler, S. Milz, Characterization of osteosarcoma cell lines MG-63, Saos-2 and U-2 OS in comparison to human osteoblasts, Anticancer Res. 24 (6) (2004) 3743–3748.
[73] N. Price, S.P. Bendall, C. Frondoza, R.H. Jinnah, D.S. Hungerford, Human osteoblast-like cells (MG63) proliferate on a bioactive glass surface, J. Biomed. Mater. Res. 37 (3) (1997) 394–400.
[74] Y. Li, J. Zhou, P. Pavanram, M.A. Leeflang, L.I. Fockaert, B. Pouran, N. Tümer, K.U. Schröder, J.M.C. Mol, H. Weinans, H. Jahr, A.A. Zadpoor, Additively manufactured biodegradable porous magnesium, Acta Biomater. 67 (2018) 378–392.
[75] J.V. Wandiyanto, V.K. Truong, M. Al Kobaisi, S. Juodkazis, H. Thissen, O. Bazaka, K. Bazaka, R.J. Crawford, E.P. Ivanova, The fate of osteoblast-like MG-63 cells on pre-infected bactericidal nanostructured titanium surfaces, Materials 12 (10) (2019).
[76] A. Srinivasan, N. Rajendran, Surface characteristics, corrosion resistance and MG63 osteoblast-like cells attachment behaviour of nano SiO2–ZrO2 coated 316L stainless steel, RSC Advances 5 (33) (2015) 26007–26016.
[77] F. Jia, S. Wang, S. Xu, W. Wu, L. Zhou, J. Zeng, The role of titanium surface micromorphology in MG-63 cell motility during osteogenesis, Sci. Rep. 12 (1) (2022) 9971.
[78] C. Padilha Fontoura, P. Ló Bertele, M. Machado Rodrigues, A. Elisa Dotta Maddalozzo, R. Frassini, C. Silvestrin Celi Garcia, S. Tomaz Martins, J.D.S. Crespo, C.A. Figueroa, M. Roesch-Ely, C. Aguzzoli, Comparative study of physicochemical properties and biocompatibility (L929 and MG63 Cells) of TiN coatings obtained by plasma Nitriding and thin film deposition, ACS Biomater. Sci. Eng. 7 (8) (2021) 3683–3695.
[79] A.M. Leferink, W.J. Hendrikson, J. Rouwkema, M. Karperien, C.A. van Blitterswijk, L. Moroni, Increased cell seeding efficiency in bioplotted three-dimensional PEOT/PBT scaffolds, J. Tissue Eng. Regen. Med. 10 (8) (2016) 679–689.
[80] S. Zhu, N. Huang, L. Xu, Y. Zhang, H. Liu, H. Sun, Y. Leng, Biocompatibility of pure iron: in vitro assessment of degradation kinetics and cytotoxicity on endothelial cells, Mater. Sci. Eng. C 29 (5) (2009) 1589–1592.
[81] R. Eid, N.T. Arab, M.T. Greenwood, Iron mediated toxicity and programmed cell death: a review and a re-examination of existing paradigms, Biochim. Biophys. Acta 1864 (2) (2017) 399–430.
[82] G. Papanikolaou, K. Pantopoulos, Iron metabolism and toxicity, Toxicol. Appl. Pharmacol. 202 (2) (2005) 199–211.
[83] T.C. Paim, D.P. Wermuth, I. Bertaco, C. Zanatelli, L.I.S. Naasani, M. Slaviero, D. Driemeier, L. Schaeffer, M.R. Wink, Evaluation of in vitro and in vivo biocompatibility of iron produced by powder metallurgy, Mater. Sci. Eng. C 115 (2020) 111129.
[84] K. Oyanagi, T. Tashiro, T. Negishi, Cell-type-specific and differentiation-status-dependent variations in cytotoxicity of tributyltin in cultured rat cerebral neurons and astrocytes, J. Toxicol. Sci. 40 (4) (2015) 459–468.
[85] S.K. Sohaebuddin, P.T. Thevenot, D. Baker, J.W. Eaton, L. Tang, Nanomaterial cytotoxicity is composition, size, and cell type dependent, Part. Fibre Toxicol. 7 (2010) 22.
[86] S. Iloki Assanga, A. Gil-Salido, L. Lewis Luján, A. Rosas-Durazo, A. Acosta-Silva, E. Rivera-Castañeda, J. Rubio-Pino, Cell growth curves for different cell lines and their relationship with biological activities, Int. J. Biotechnol. Mol. Biol. Res. 4 (4) (2013) 60–70.
[87] M.S. Mohamed, S. Veeranarayanan, H. Minegishi, Y. Sakamoto, Y. Shimane, Y. Nagaoka, A. Aki, A.C. Poulose, A. Echigo, Y. Yoshida, T. Maekawa, D.S. Kumar, Cytological and subcellular response of cells exposed to the Type-1 RIP curcin and its hemocompatibility analysis, Sci. Rep. 4 (1) (2014) 5747.

[88] L. Mok, J.W. Wynne, S. Grimley, B. Shiell, D. Green, P. Monaghan, J. Pallister, A. Bacic, W.P. Michalski, Mouse fibroblast L929 cells are less permissive to infection by Nelson Bay orthoreovirus compared to other mammalian cell lines, J. Gen. Virol. 96 (Pt 7) (2015) 1787–1794.
[89] Y. Kubo, C.J. Wruck, A. Fragoulis, W. Drescher, H.C. Pape, P. Lichte, H. Fischer, M. Tohidnezhad, F. Hildebrand, T. Pufe, H. Jahr, Role of Nrf2 in fracture healing: clinical aspects of oxidative stress, Calcif. Tissue Int. (2019).
[90] D.J. Kosman, Iron metabolism in aerobes: managing ferric iron hydrolysis and ferrous iron autoxidation, Coord. Chem. Rev. 257 (1) (2013) 210–217.
[91] M. Schinhammer, I. Gerber, A.C. Hänzi, P.J. Uggowitzer, On the cytocompatibility of biodegradable Fe-based alloys, Mater. Sci. Eng. C 33 (2) (2013) 782–789.
[92] T. Huang, Y. Zheng, Uniform and accelerated degradation of pure iron patterned by Pt disc arrays, Sci. Rep. 6 (2016) 23627.
[93] T. Huang, J. Cheng, D. Bian, Y. Zheng, Fe–Au and Fe–Ag composites as candidates for biodegradable stent materials, J. Biomed. Mater. Res. B 104 (2) (2016) 225–240.
[94] J. He, F.-L. He, D.-W. Li, Y.-L. Liu, D.-C. Yin, A novel porous Fe/Fe-W alloy scaffold with a double-layer structured skeleton: preparation, in vitro degradability and biocompatibility, Colloids Surf. B 142 (2016) 325–333.
[95] A. Purnama, H. Hermawan, J. Couet, D. Mantovani, Assessing the biocompatibility of degradable metallic materials: state-of-the-art and focus on the potential of genetic regulation, Acta Biomater. 6 (5) (2010) 1800–1807.
[96] R. Oriňaková, A. Oriňak, M. Giretová, L.u. Medvecký, M. Kupková, M. Hrubovčáková, I. Maskal'ová, J. Macko, F. Kal'avský, A study of cytocompatibility and degradation of iron-based biodegradable materials, J. Biomater. Appl. 30 (7) (2016) 1060–1070.
[97] W.H. De Jong, J.W. Carraway, R.E. Geertsma, 6 - In vivo and in vitro testing for the biological safety evaluation of biomaterials and medical devices, in: J.P. Boutrand (Ed.), Biocompatibility and Performance of Medical Devices, second ed., Woodhead Publishing, 2020, pp. 123–166.
[98] E. Scarcello, A. Herpain, M. Tomatis, F. Turci, P.J. Jacques, D. Lison, Hydroxyl radicals and oxidative stress: the dark side of Fe corrosion, Colloids Surf. B 185 (2020) 110542.
[99] G. Kroemer, W.S. El-Deiry, P. Golstein, M.E. Peter, D. Vaux, P. Vandenabeele, B. Zhivotovsky, M.V. Blagosklonny, W. Malorni, R.A. Knight, M. Piacentini, S. Nagata, G. Melino, Classification of cell death: recommendations of the Nomenclature Committee on Cell Death, Cell Death Different. 12 (2005) 1463.
[100] D.J. Taatjes, B.E. Sobel, R.C. Budd, Morphological and cytochemical determination of cell death by apoptosis, Histochem. Cell Biol. 129 (1) (2008) 33–43.
[101] N. Mohd Daud, N.B. Sing, A.H. Yusop, F.A. Abdul Majid, H. Hermawan, Degradation and in vitro cell–material interaction studies on hydroxyapatite-coated biodegradable porous iron for hard tissue scaffolds, J. Orthop. Transl. 2 (4) (2014) 177–184.
[102] J. Farack, C. Wolf-Brandstetter, S. Glorius, B. Nies, G. Standke, P. Quadbeck, H. Worch, D. Scharnweber, The effect of perfusion culture on proliferation and differentiation of human mesenchymal stem cells on biocorrodible bone replacement material, Mater. Sci. Eng. B 176 (20) (2011) 1767–1772.
[103] M.A. Gillissen, E. Yasuda, G. de Jong, S.E. Levie, D. Go, H. Spits, P.M. van Helden, M.D. Hazenberg, The modified FACS calcein AM retention assay: a high throughput flow cytometer based method to measure cytotoxicity, J. Immunol. Methods 434 (2016) 16–23.
[104] S. Buracco, B. Peracino, R. Cinquetti, E. Signoretto, A. Vollero, F. Imperiali, M. Castagna, E. Bossi, S. Bozzaro, Dictyostelium Nramp1, which is structurally and functionally similar to mammalian DMT1 transporter, mediates phagosomal iron efflux, J. Cell Sci. 128 (17) (2015) 3304–3316.
[105] Y. Ma, V. Abbate, R.C. Hider, Iron-sensitive fluorescent probes: monitoring intracellular iron pools, Metallomics 7 (2) (2014) 212–222.
[106] C. Kirchhoff, H. Cypionka, Propidium ion enters viable cells with high membrane potential during live-dead staining, J. Microbiol. Methods 142 (2017) 79–82.
[107] J. Wang, L. Liu, Y. Wu, M.F. Maitz, Z. Wang, Y. Koo, A. Zhao, J. Sankar, D. Kong, N. Huang, Y. Yun, Ex vivo blood vessel bioreactor for analysis of the biodegradation of magnesium stent models with and without vessel wall integration, Acta Biomater. 50 (2017) 546–555.